UCLouvain

École polytechnique de Louvain

High gain X-band space antenna capable of beamsteering

Author: **Arthur Romeijer**
Supervisor: **Christophe Craeye**
Readers: **Dimitri Lederer, Sumit Karki, Thomas Pairon**
Academic year 2020–2021
Master [120] in Electrical Engineering

Abstract

Small satellites orbiting in low-Earth orbits enable new applications requiring the transfer of information between the satellites and ground stations. However, such a system demands both a substantial signal-to-noise ratio at the receiver and broad system bandwidth to have good data throughput. Therefore, the goal of this master thesis is to study a high gain X-band beamsteering-capable space antenna to improve the system signal-to-noise ratio. Furthermore, the system scan requirement is broad to maximize the link availability duration. This work is a collaboration with Aerospacelab, active in geospatial intelligence.

Worst-case analysis of the link budget sets the requirements to close the link and predicts the achievable spectral efficiency. It fixes a minimum directivity of 10.2 dBi for the antenna.

We studied conformal phased array antennas to accommodate the high scan requirement. Nevertheless, planar phased arrays maximize the performance for this application while limiting the manufacturing complexity.

Selecting the beamformers and power dividers sets the minimum radio-frequency input power (0.048 W) and DC supply power (28.8 W) for the antenna. We made a first layout proposal based on several considerations.

Finally, we designed an aperture-coupled antenna with a specific microstrip-to-stripline transition to avoid using blind vias. It has a 6.4% impedance bandwidth and linear polarization. Sequential rotation of the antennas in a two-by-two array improves the axial ratio of the system, which targets a circular polarization.

This microstrip-to-stripline transition through coupling enables feeding the antennas without requiring blind vias. In an environment like space where significant thermal expansion provokes mechanical stress on the structure, such a transition is of interest as it improves the system's robustness.

Acknowledgements

I want to express my deep gratitude to my supervisors, Prof. Christophe Craeye, Sumit Karki, and Thomas Pairon, for their constant support and excellent advice throughout the year.

I also want to sincerely thank Isabelle Huynen for her helpful expertise for the microstrip-to-stripline transition, Brigitte Dupont for the installation of CST STUDIO SUITE on Linux servers and Husnain Ali Kayani for his CST tutorial.

Finally, I want to thank my parents, friends, and girlfriend for their love and support.

Summary

List of Acronyms

APSK Amplitude and Phase-Shift Keying. 14

AR Axial Ratio. 7, 22

AWGN Additive White Gaussian Noise. 16

BCH Bose-Chaudhuri-Hocquenghem. 15

BER Bit Error Rate. 14

C/N Carrier to Noise ratio. 16

CP Circular Polarization. 7, 18, 52–55, 65

CPA Cylindrical Phased Array. 27, 28

CST CST STUDIO SUITE by 3ds. 29, 52, 66, 75

DVB-S2 Digital Video Broadcast Second Generation. 14, 15

ITU International Telecommunication Union. 11, 20

LDPC Low-Density Parity Check. 15

LEO Low Earth Orbit. 10, 47

LHCP Left-Handed Circular Polarization. 6, 7

MS-MS Microstrip-to-Microstrip. 56–62

MS-SL Microstrip-to-Slotline. 56

PCB Printed Circuit Board. ii, 46–50

PSK Phase-Shift Keying. 14

QPSK Quadrature Phase-Shift Keying. 14

RF Radio Frequency. 42–46, 48, 49

RHCP Right-Handed Circular Polarization. 6, 7, 12, 18, 19

SNR Signal-to-Noise Ratio. 10, 14, 15, 21, 22, 74

SvalSat Svalbard Satellite Station. 10

TX Transmitter. 35, 43–45

1 | Introduction

Small satellites orbiting in low-Earth orbit enable new applications like broadband and low-latency internet access worldwide. This document targets a similar mission and collaborates with Aerospacelab, a company active in geospatial intelligence. Their in-house designed satellites fly in low Earth orbits, capture images of the Earth and send those wirelessly to a ground station for post-processing.

The application requires a sufficiently high signal-to-noise ratio at the receiver to close the link and to have a high payload data downlink to the ground. The system can use a high-gain antenna to increase it, which requires ground station tracking as it creates a spatially selective beam. The company chooses to avoid mechanical pointing for the satellite's antenna to reduce the system complexity, which implies designing a phased array antenna capable of beamforming. The radio-frequency antenna system targets an X-band operating frequency, a broad bandwidth, a circular polarization, and a wide scan range to maximize the link availability duration.

The conception of such an antenna implies multiple challenges starting with the strong requirement in terms of scan angle. During the design, we considered a conformal phased array antenna. This technique allows boosting the directivity for low grazing angles. However, it implies that the structure hides some antennas for certain look angles, which reduces the available power at the transmitter, degrading the link budget. We also selected part of the electronic circuits required for the radio frequency communication chain. Finally, we discussed some layout considerations and proposed an antenna design with a specific microstrip-to-stripline transition, avoiding the use of blind vias.

This work investigates the achievable data throughput, the shape of the phased array, the integrated circuits required by the communication chain, the layout, and the antenna with a microstrip-to-stripline transition. First, Chapter 2 presents an antenna overview to remind aspects of the antenna theory. Chapter 3 gives the different system requirements, which will serve as the basis for the link budget. Next, Chapter 4 studies the system link budget, allowing a prediction about the

achievable system throughput. Then, Chapter 5 investigates the best shape for the phased array antenna, giving a comprehensive comparison between two different conformal phased array antennas and one planar phased array antenna. Chapter 6 aims to select the beamformers and the power dividers, estimate the power requirements, and give layout considerations. Finally, Chapter 7 examines the design of an X-band antenna suitable for this application and the placement of such antenna in a two-by-two array using sequential rotation to improve the axial ratio of the system.

2 | Antenna overview

Antennas are passive circuit elements enabling the radiation of electromagnetic waves in space. Reciprocally, it allows capturing ambient electromagnetic waves and transfers a signal to the underlying electronics. Such element finds various applications such as wireless communication between devices, radar application, astronomy, and, more recently, wireless power transmission toward low power devices (energy harvesting). When studying those systems, several characteristics are of interest. This chapter gives an overview of antenna design and presents valuable concepts for the rest of this work.

2.1 System of coordinates

We will mainly use a spherical coordinate system during this work, defining any point in space using three components: the angle θ, the angle ϕ, and the radial distance r. We will name the angle θ, the elevation angle, and ϕ, the azimuth angle. Figure 2.1 gives a representation of the coordinate system.

We will also map the spherical coordinates to U-V coordinates. It gives a two-dimensional representation of the positive hemisphere ($\theta \leq 90°$). The mapping is as:

$$u = \sin(\theta)\cos(\phi) \tag{2.1}$$

$$v = \sin(\theta)\sin(\phi) \tag{2.2}$$

2.2 Reciprocity

The reciprocity principle is a crucial property of antenna theory. It allows linking the different antenna's characteristics in transmit and receive. For instance, after characterizing the antenna's radiation pattern in transmit, the same radiation pattern is valid in receive too.

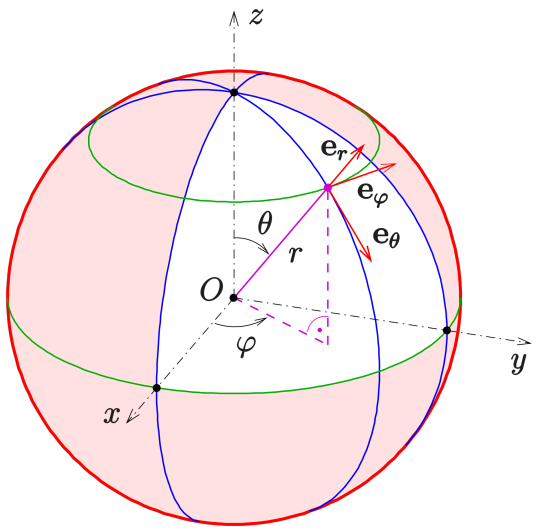

Figure 2.1: From [1]: Spherical coordinate system.

2.3 Radiation pattern

An antenna radiates electromagnetic waves from current excitation flowing through the structure. Integration over the antenna's volume of these infinitesimal current contributions allows computing the generated electric field at a given position in space. We can express the resulting electric field as:

$$\mathbf{E}(\mathbf{r}) = -\frac{j\eta}{2\lambda}\frac{e^{-jkR}}{R}\int_V (\mathbf{J}(\mathbf{r}') - \hat{u}\mathbf{J}(\mathbf{r}')\cdot\hat{u})\, e^{jk\hat{u}\cdot\rho} dV' \tag{2.3}$$

In Equation 2.3, $\mathbf{E}$ is the electric field, j is the imaginary number, η is the free-space impedance, λ is the wavelength, and $\mathbf{J}$ is the current distribution. Figure 2.2 gives a geometrical representation of the problem and a definition of the other quantities. This expression simplifies under the far-field assumption, implying that the observer is sufficiently far away from the antenna. That is: $R >> \lambda$, $R >> D$, and $R >> 2D^2/\lambda$, with D the largest antenna's dimension. Under this assumption, we can re-write Equation 2.3 as:

$$\mathbf{E}(\mathbf{r}) = \frac{e^{-jkR}}{R}\mathbf{F}(\hat{u}) \tag{2.4}$$

In Equation 2.4, $\mathbf{F}(\hat{u})$ is the antenna's radiation pattern. That quantity gives the field intensity of the antenna solely based on the direction of observation. Figure 2.3 gives a two-dimensional example (cut of a three-dimensional radiation pattern). We notice that it has a main beam and several sidelobes. It also defines the half-power beamwidth and the null beamwidth.

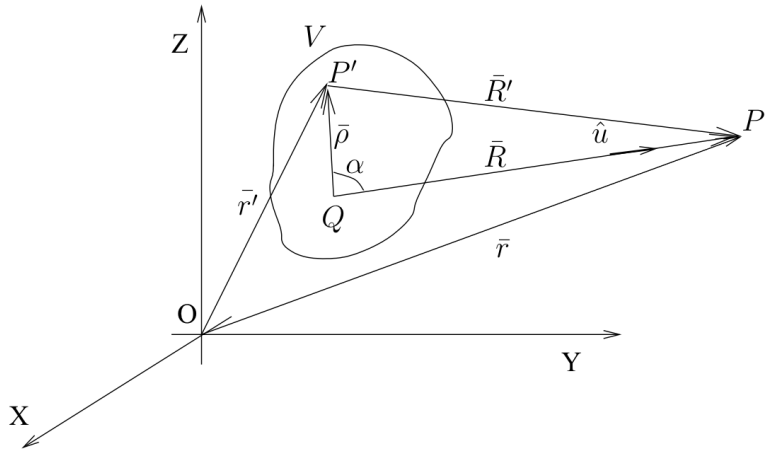

Figure 2.2: From [2]: Geometry for field computation based on the current distribution J over a volume V.

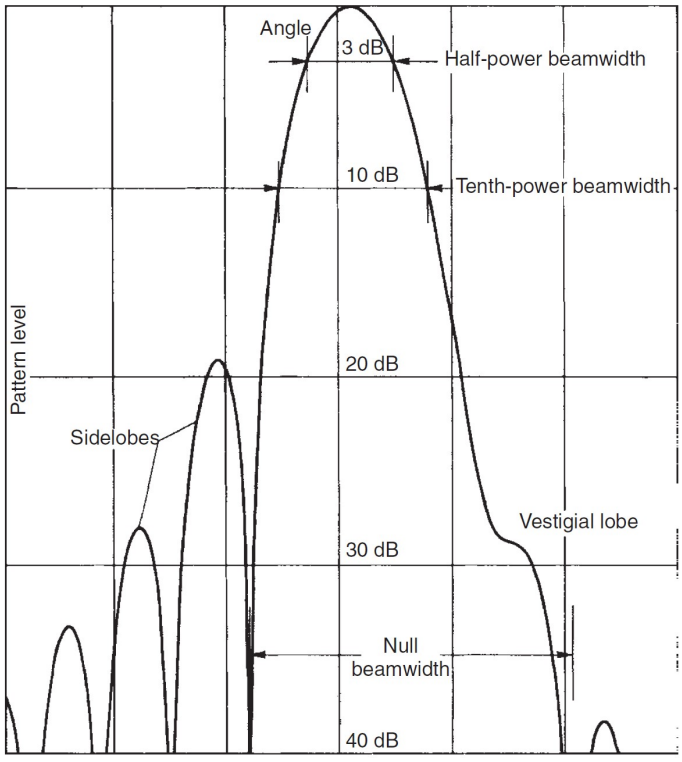

Figure 2.3: From [3]: Radiation pattern characteristics.

2.4 Directivity

Directivity is one of the primary radiation pattern's figures of merit. It defines the selectivity of the antenna, the gain of the antenna in a specific direction. It corresponds to the ratio between the power density of the system in a specific direction and the power density of an isotropic radiator with equivalent power. We commonly express this gain in dBi (decibels-isotropic).

$$D(\hat{u}) \triangleq \frac{S(\hat{u})}{\left(\frac{P_r}{4\pi R^2}\right)} = 4\pi \frac{|\mathbf{F}(\hat{u})|^2}{\int\int |\mathbf{F}(\hat{u})|^2 \, d\Omega'} \tag{2.5}$$

$$D(\hat{u}) \text{ (dBi)} = 10 \log_{10}(D(\hat{u})) \tag{2.6}$$

2.5 Polarization and axial ratio

The wave polarization is the direction of the electric field. In the far-field, where the electric field only has components perpendicular to the direction of propagation, we can see the wave propagation as a planar wave. We can decompose the electric field into its ϕ and θ components in this plane, as represented in Figure 2.1. Let us write the electric field decomposition as:

$$\mathbf{E} = E_\theta \hat{\theta} + E_\phi \hat{\phi} \tag{2.7}$$

During this work, the system targets Right-Handed Circular Polarization (RHCP) ($\hat{R}$). Left-Handed Circular Polarization (LHCP) ($\hat{L}$) also exists and is orthogonal with the latter. We can define these two polarizations from linear components as:

$$\hat{R} = \frac{1}{\sqrt{2}}(\hat{\theta} - j\hat{\phi}) \tag{2.8}$$

$$\hat{L} = \frac{1}{\sqrt{2}}(\hat{\theta} + j\hat{\phi}) \tag{2.9}$$

We can then express the electric field as a sum of its right and left-handed circular polarization components [3]:

$$\mathbf{E} = E_L \hat{L} + E_R \hat{R} \tag{2.10}$$

$$E_L = \mathbf{E} \cdot \hat{L}^* \tag{2.11}$$

$$E_R = \mathbf{E} \cdot \hat{R}^* \tag{2.12}$$

As those two bases are orthogonal, if $\mathbf{E}$ has a perfectly right-handed circular polarization, its E_L component will be zero. From there, we can introduce a new

quantity, the Axial Ratio (AR). This metric allows checking the quality of the Circular Polarization (CP). We define the RHCP and LHCP axial ratios as [3]:

$$\text{AR} = \frac{|E_R| + |E_L|}{|E_R| - |E_L|} \quad \text{RHCP} \tag{2.13}$$

$$\text{AR} = \frac{|E_L| + |E_R|}{|E_L| - |E_R|} \quad \text{LHCP} \tag{2.14}$$

$$\text{AR (dB)} = 20\log_{10}(\text{AR}) \tag{2.15}$$

For perfect RHCP or LHCP, the axial ratio is equal to 0 dB.

2.6 S-parameters

A scattering matrix is a necessary formalism for microwave circuits. Indeed, defining voltages and currents for non-transverse electromagnetic lines is difficult. Measuring voltage and current at microwave frequencies is also a challenge because direct measurements involve the magnitude and phase of a travelling or standing wave. The scattering matrix represents direct measurements and gives ideas of the incident, reflected, and transmitted waves. It gives a complete description of any N-port network by relating the incident voltage waves on the ports to those reflected by the ports [4].

$$\begin{bmatrix} V_1^- \\ V_2^- \\ \vdots \\ V_N^- \end{bmatrix} = \begin{bmatrix} S_{11} & S_{12} & \dots & S_{1N} \\ S_{21} & \ddots & & \vdots \\ \vdots & & \ddots & \vdots \\ S_{N1} & \dots & \dots & S_{NN} \end{bmatrix} \begin{bmatrix} V_1^+ \\ V_2^+ \\ \vdots \\ V_N^+ \end{bmatrix} \tag{2.16}$$

$$S_{ij} = \left.\frac{V_i^-}{V_j^+}\right|_{V_k^+ \text{ for } k \neq j} \tag{2.17}$$

For instance, the S_{11} parameter gives the reflection coefficient for a two-port network. We can express it as:

$$S_{11} = \left.\frac{V_1^-}{V_1^+}\right|_{V_2^+ = 0} = \left.\Gamma^{(1)}\right|_{V_2^+ = 0} \tag{2.18}$$

For a lossless structure, the following property holds:

$$\sum_{k=1}^{N} S_{ki} S_{ki}^* = 1 \tag{2.19}$$

When placing an antenna in an array, it interacts with the other elements. The interactions highly depend on the different elements' excitation phase shifts, which

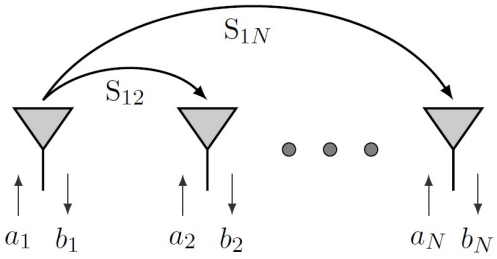

Figure 2.4: From [5]: N elements antenna array.

motivates the usage of the active impedance formalism. The term active comes from the interactions between the different elements. Figure 2.4 depicts the interplay between antennas through the different S-parameters. It considers an N elements antenna array with the incident and reflected voltages.

The i^{th} element reflected voltage, which accounts for mutual coupling, is as [5]:

$$V_i^- = S_{i1}V_1^+ + ...S_{1i}V_i^+ + ... + S_{iN}V_N^+ \tag{2.20}$$

The active impedance of that same element is the ratio between the incident and reflected voltages when we fully excite the antenna array. That is:

$$S_{ii} = \frac{V_i^-}{V_I^+} = \frac{\sum_{n=1}^{N} S_{in}V_n^+}{V_i^+} \tag{2.21}$$

2.7 Beamforming

We can scan a beam electronically using a technique called beamforming. Several antennas compose the antenna module. Applying a specific phase shift to each antenna allows for the difference in propagation distance compensation and achieving constructive interference in a specific direction [2]. We first need to introduce the superposition principle. Thanks to the linearity of Maxwell's equations, the equivalent electric field at a point in space is simply the sum of the different antenna contributions. It is essential to mention that those may vary when we place the antennas close to each other in a network due to mutual coupling. We then care about the antenna pattern in the presence of the other antennas.

$$\mathbf{E} = \sum_{n=1}^{N} \mathbf{E}_n \tag{2.22}$$

The electric field radiated by the antenna follows the relation in Equation 2.4 in the far-field. Taking two antennas, we want to sum their radiated electric fields at a

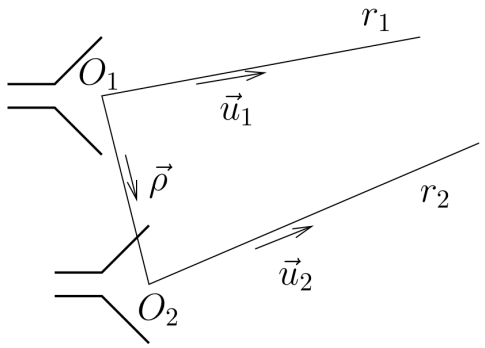

Figure 2.5: From [2]: Translation principle example.

point far from them. Looking at Figure 2.5 and using the Fraunhofer approximation allows us to write:

$$\mathbf{u}_1 \approx \mathbf{u}_2 \approx \mathbf{u} \tag{2.23}$$

$$\mathbf{r}_2 \approx \mathbf{r}_1 - \rho \cdot \mathbf{u} \tag{2.24}$$

$$\frac{1}{r_2} e^{-jkr_2} \approx \frac{1}{r_1} e^{-jkr_1} e^{jk\rho \cdot \mathbf{u}} \tag{2.25}$$

$$\mathbf{E}_2 \approx \mathbf{E}_1 e^{jk\rho \cdot \mathbf{u}} \tag{2.26}$$

In Equation 2.24, we notice that the difference in magnitude between $\mathbf{r}_1$ and $\mathbf{r}_2$ is small and thus negligible in the denominator. For the argument of the complex exponent, on the other hand, the phase difference is considerable. We thus need to have a phase factor to compensate for it. We can put the radiation pattern in evidence for a planar antenna array when summing the electric field from the different antennas. It allows us to write an equivalent radiation pattern as:

$$\mathbf{F}(\mathbf{u}) = \mathbf{F}_0(\mathbf{u}) \sum_n \alpha_n e^{j\beta_n} e^{jk\rho_n \cdot \mathbf{u}} \tag{2.27}$$

In Equation 2.27, α_n is the amplitude, and β_n is the phase shift applied to the antenna element number n. The designer uses those two parameters to steer the beam in a particular direction by creating a constructive interference between the contributions. We obtain that by compensating for the phase difference that stems from the difference between propagation distances for a planar array.

3 System requirements

3.1 Application target

The mission targets a Low Earth Orbit (LEO), with an altitude of 500 km. From there, a small satellite will orbit and transfer data to a ground station. The antenna system, which is the focus of this work, aims at establishing a communication link between the satellite and the ground station. As the application requires a high payload data downlink to the ground, we require a sufficiently high Signal-to-Noise Ratio (SNR) at the receiver such that the system can use a higher-order modulation scheme. That is why the system requires a high gain and beam steering towards the ground station as it flies above it in orbit. The initial gain requirement is 18 dB over the whole scan range.

3.2 Ground station

We will consider the Svalbard Satellite Station (SvalSat) as the satellite ground station during this work. This facility supports L, S, C, X, and K bands. Table 3.1 lists several of its characteristics. Part of this data comes from Reference [6]. The G/T metric is valid for an elevation of 20° above the horizon.

3.3 Operational requirements

This section will gather the different operational requirements. Those are available in Table 3.1, along with the different mission's orbit parameters. We will give additional details about the frequency and scan requirements.

3.3.1 Frequency requirements

The system needs to operate in the X-band, which ranges from 8 to 12 GHz. More precisely, the antenna shall transmit in the frequency range between 8025 and 8400

MHz for this application, corresponding to the band reserved by the International Telecommunication Union (ITU) for Space-to-Earth operation. That gives us a system bandwidth of 375 MHz, close to 4.5 % of the operating frequency.

3.3.2 Scan requirements

We have to scan the beam electronically. Indeed, we do not allow mechanical pointing of the antenna module as it adds extra complexity to the system and a single-point-of-failure. In addition, we should not block the module's field of view with any other component of the satellite. The antenna module needs an elevation scan, θ going from 0 to 65°, and a full azimuth scan, ϕ going from 0 to 360°. Those angles are defined in Figure 2.1. The angular range is broad to maximize the communication duration between the satellite and the ground station. We require a full azimuth scan as the satellite will not always fly strictly above the ground station. We will compute the elevation scan requirement by solving a geometric problem.

Figure 3.1 describes this scenario. In that figure, R_E is the Earth radius (6371 km), h_s is the satellite's orbit distance from Earth, h_a is the ground station elevation, θ is the antenna system look angle, ϵ is the ground station elevation angle, and d is the distance between the satellite and the ground station. The minimum elevation angle corresponds to when the satellite initiates the communication link and starts the beam tracking. As some physical obstacles like trees may block the field of view, we will choose a typical ϵ of 10°. Solving this problem allows isolating the maximum antenna look angle. The solution is in Reference [7]:

$$\theta = \text{asin}\left(\frac{\cos(\epsilon)(R_E + h_a)}{R_E + h_s}\right) \tag{3.1}$$

By introducing the numerical values into Equation 3.1, it gives $\theta = 65.94°$. That value sets the maximum scan angle of our system.

3.4 Design requirements

Table 3.1 lists the system design requirements. Those refer to radiation pattern characteristics. They also include the physical requirements for the antenna.

Requirement	Value	Unit
Satellite ground station parameters		
Longitude	15.3975103	°
Latitude	78.2297492	°
Elevation sea level	458	m
X-band G/T	26.5	dB/K
Antenna dish diameter	3.7	m
Orbit parameters		
Orbit type	circular	-
Orbit inclination	98	°
Orbit altitude	500	km
System operational requirements		
Frequency range	8025-8400	MHz
Bandwidth	375	MHz
θ scanning range	0-65	°
Scanning precision	1	°
System design requirements		
Copolar gain	18	dBi
Maximum azimuthal gain variation	1	dB
Polarization	RHCP	-
Axial ratio	3	dB
Maximum physical size	$150 \times 150 \times 100$	mm × mm × mm

Table 3.1: System requirements.

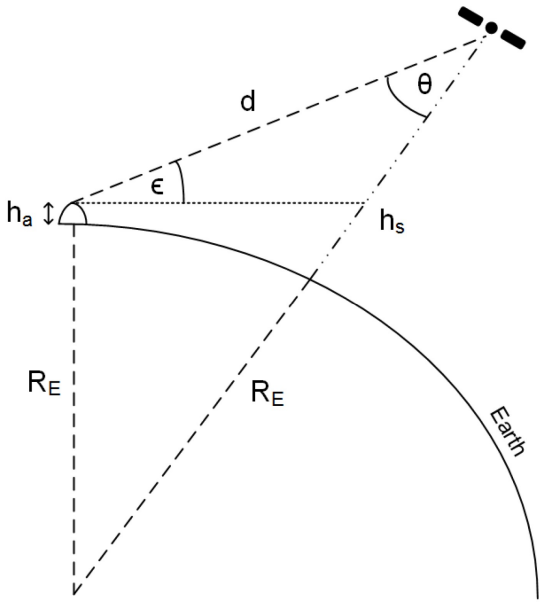

Figure 3.1: From [7]: Relative position of the satellite and the ground station at the farthest communicative distance.

4 | System link budget

A proper link budget analysis is crucial to ensure the link feasibility under various conditions. It will allow cross-validation of the specifications mentioned in Chapter 3. For a specific technology choice, bit rate computation is possible using the SNR and the bandwidth of the system. This chapter focuses on establishing this link budget and discusses the different system requirements.

Section 4.1 will introduce the Digital Video Broadcast Second Generation (DVB-S2) standard, give its Bit Error Rate (BER) requirements, and yield the associated achievable bit rate. In Section 4.2, we will identify and analyze the different system loss origins. In Section 4.3, we will analyze the system noise and link it to the system bandwidth. Finally, in Section 4.4, we will introduce the transmission power to allow the global link budget. We will perform a worst-case analysis during this work to make sure that the link is achievable in all foreseen circumstances.

4.1 Standard overview and BER requirements

To set the BER requirements appropriately, we need to analyze the communication chain and fix parameters such as the modulation, the coding, and the roll-off factor. The DVB-S2 standard is for multimedia broadcasting by satellites. We will use the release TR 102 376-1 throughout this work [8]. For the sake of completeness, we will present the Amplitude and Phase-Shift Keying (APSK) modulation and the coding scheme. Finally, we will include a graph of the achievable rate versus SNR.

4.1.1 Modulation scheme

The DVB-S2 standard uses four constellations: Quadrature Phase-Shift Keying (QPSK), Phase-Shift Keying (PSK) 8, APSK 16, and APSK 32 (showcased in Figure 4.1). The system can hop from one constellation to the other to relax the SNR requirements by reducing the constellation order while lowering throughput. Those modulation schemes offer intrinsic robustness against non-linear amplifiers' distortions and good spectral efficiency [9]. They are thus perfectly adapted for

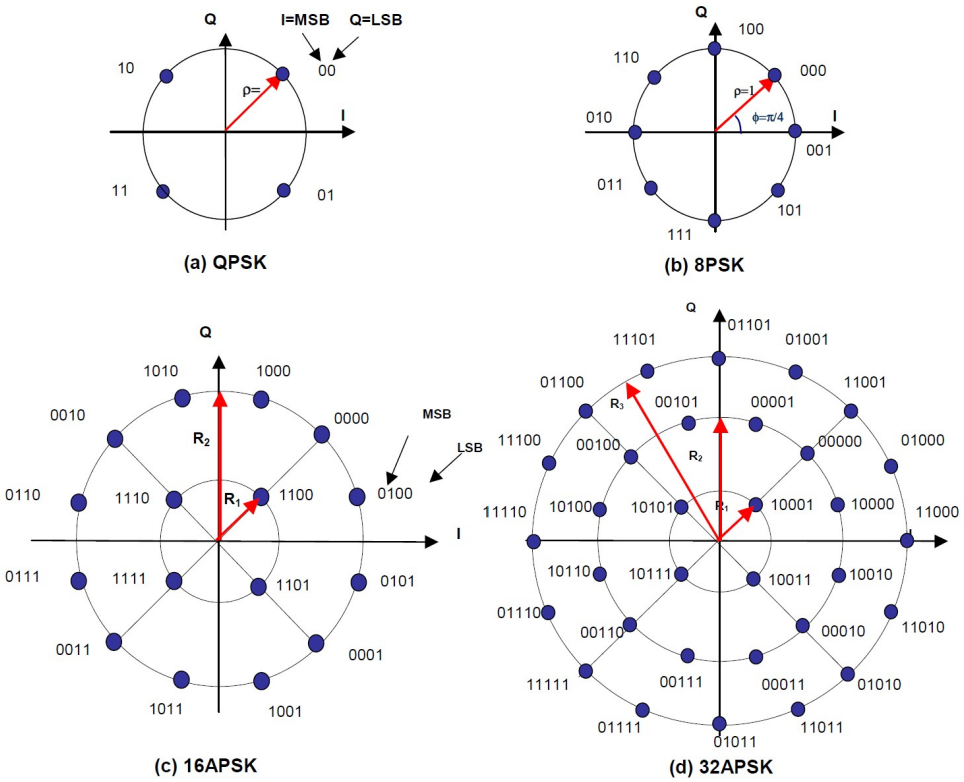

Figure 4.1: From [8]: The four possible DVB-S2 modulation schemes and their respective constellations.

satellite communication applications.

4.1.2 Coding scheme

The standard uses a concatenation of Bose-Chaudhuri-Hocquenghem (BCH) and Low-Density Parity Check (LDPC) codes [8]. BCH codes are block codes meaning it requires that we transmit the information in packets with a length of K symbols. The coding efficiency becomes more significant as the packet length increases. Its goal is to avoid unwanted error floors at high SNR. LDPC codes are linear block codes and support highly parallelized decoding procedures (parity-check equations with many iterations) [10]. The DVB-S2 standard fixes the LDPC code block length to 64800 bits for a standard frame and supports 50 decoding iterations.

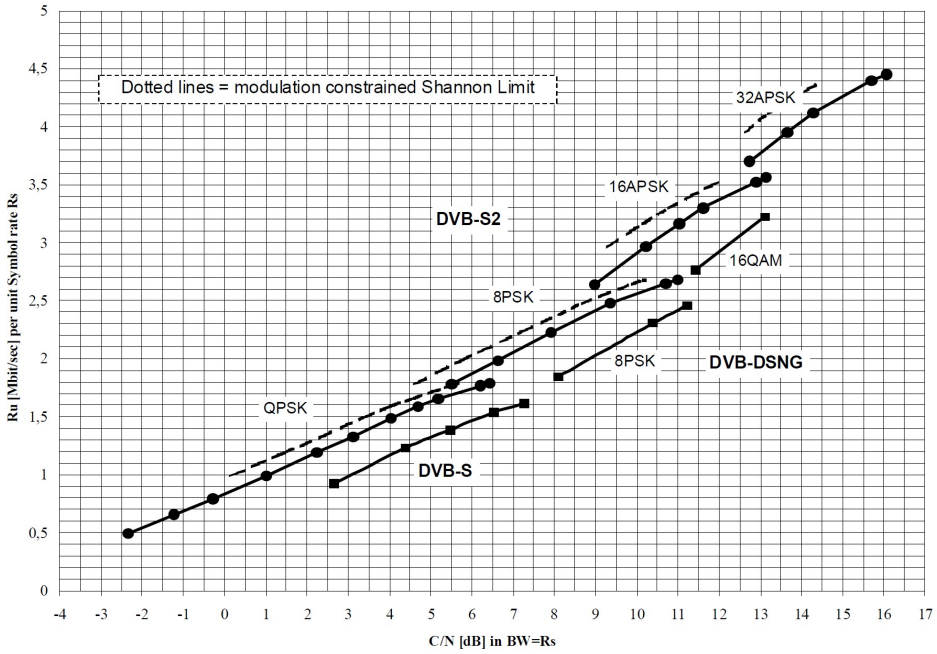

Figure 4.2: From [8]: Required C/N versus spectrum efficiency for the four DVB-S2 modulation schemes and various coding rates.

4.1.3 Achievable rate

Let us start by stating that the system operation targets a quasi-error-free operation. That represents a packet error rate of 10^{-7}. The standard fixes the packet length to 188 bytes, translating into a BER of less than 10^{-10} to 10^{-11}. Figure 4.2 gives the required Carrier to Noise ratio (C/N) (measured in a bandwidth equal to the symbol rate), equivalent to an SNR for the carrier, versus the spectrum efficiency (effective bit rate per unit symbol rate). The system can operate with C/N from -2.4 dB (QPSK with 1/4 coding rate) to 16 dB (32APSK with 9/10 coding rate). The curve is valid under the Additive White Gaussian Noise (AWGN) channel assumption.

4.2 Transmission losses

Several effects will affect the Earth-satellite communication link. Some of them are time and location-dependent, such as the additional losses coming from heavy rain. Thus, it is essential to determine the location of the ground station before analyzing the link. Other parameters of the system, such as the operating frequency, will also play an important role. This section presents a non-exhaustive list of loss sources.

4.2.1 Free space losses

Free space losses are the most significant source of losses. It comes from the power density (in $\frac{W}{m^2}$) reduction due to the spread of finite power over a growing surface. That power density translates into the received power after multiplication with the receiver's effective area.

$$S = \frac{P_T G_T}{4\pi r^2} \tag{4.1}$$

$$P_R = \frac{P_T G_T A_{eR}}{4\pi r^2} \tag{4.2}$$

$$G_R = \frac{4\pi}{\lambda^2} A_{eR} \tag{4.3}$$

Grouping those equations together leads to the free space loss definition:

$$L_{FS} = \frac{P_T G_T G_R}{P_R} = \left(\frac{4\pi r}{\lambda}\right)^2 \tag{4.4}$$

In Equations 4.1 to 4.4, L_{FS} is the free space loss, S is the power density, P_T is the transmitted power, P_R is the received power, G_T is the gain in transmit, G_R is the gain in receive, r is the distance expressed in meters, λ is the wavelength, and A_{eR} is the receiver's effective area. At this stage, we need to compute the maximal distance between the satellite and the ground station for our worst-case analysis. Reference [11] gives a solution to address this problem:

$$d_{max} = R_E \frac{\sin\left(\frac{\pi}{2} - \epsilon_{min} - \text{asin}\left(\frac{R_E}{R_E + h_s}\cos(\epsilon_{min})\right)\right)}{\frac{R_E}{R_E + h_s}\cos(\epsilon_{min})} \tag{4.5}$$

From Equations 4.4 and 4.5, we can compute the maximal distance and the corresponding losses. Figure 4.3 gives the evolution of the free space losses versus the propagation distance at 8.4 GHz. The maximal distance between the ground station and the satellite for this application is 1694.6 km, translating into a loss of 175.5 dB for a frequency of 8.4 GHz.

4.2.2 Attenuation by rain

Attenuation by rain comes from the scattering of electromagnetic waves by a random distribution of various-sized water droplets. This attenuation varies with frequency and rain rate expressed in mm per hour. We are interested in the rain statistics of the ground station because computing the attenuation requires fixing a rain rate. Typically, we target a link availability of 99.99% of the time, such

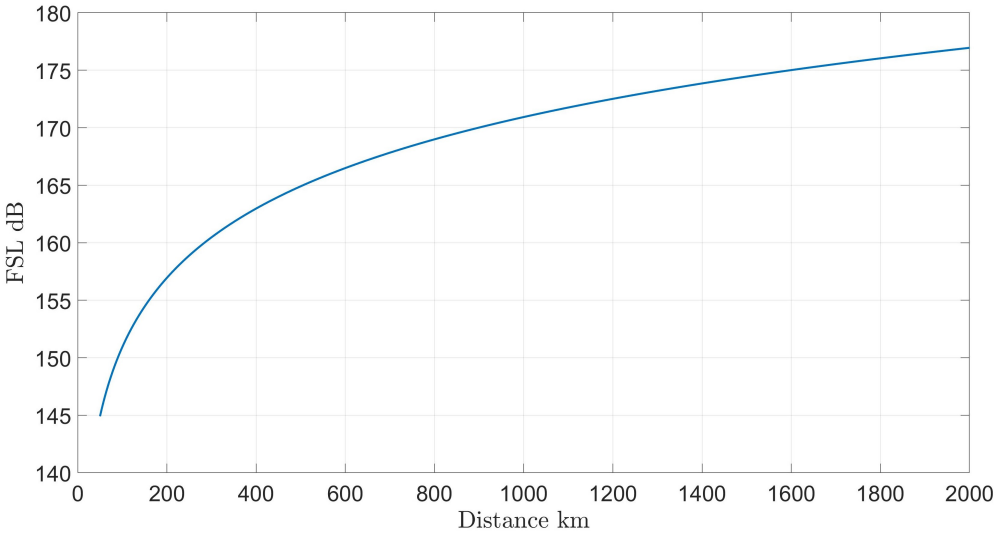

Figure 4.3: Free space losses vs. propagation distance at 8.4 GHz.

that the location's rain rate does not exceed that level for more than 0.01% of the time. The International Telecommunication Union provides recommendations to compute those attenuations. Recommendation P.838-3 [12] gives the procedure to compute the specific attenuation γ_R in dB per km, and recommendation P.837-7 [13] gives the 0.01% rain rate.

$$\gamma_R = kR^{\alpha} \tag{4.6}$$

In Equation 4.6, k and α are fitting parameters available in Reference [12]. R is the 0.01% rain rate, which is about 10 mm/h in Svalbard. It gives a specific attenuation of 0.092 dB/km. The maximal path length affected by rain is close to 9 km. We will thus consider a rain attenuation L_{rain} of 0.82 dB.

4.2.3 Polarization losses

The system targets RHCP polarization. Nevertheless, perfect CP is not achievable, and polarization mismatch is present. The polarization mismatch introduces an additional loss, depending on the antenna module's axial ratio. Chapter one of Reference [3] and Reference [14] present the computation procedure.

$$L_{pol}\ (\text{dB}) = 10\log_{10}\left(\frac{1+|\rho_W|^2|\rho_A|^2+2|\rho_W||\rho_A|\cos(2\theta)}{(1+|\rho_W|^2)(1+|\rho_A|^2)}\right) \tag{4.7}$$

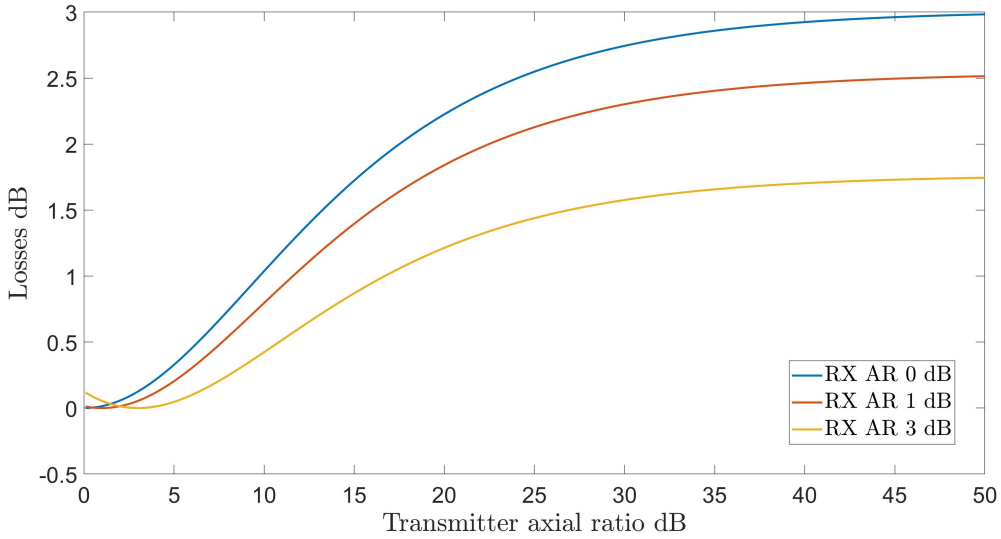

Figure 4.4: Polarization losses vs. transmitter axial ratio for various receiver axial ratios (0, 1, 3 dB).

$$|\rho_W| = \frac{r_W + 1}{r_W - 1} \tag{4.8}$$

$$|\rho_A| = \frac{r_A + 1}{r_A - 1} \tag{4.9}$$

In Equations 4.7 to 4.9, L_{pol} is the polarization mismatch loss in dB, r_W is the incident wave's axial ratio in natural units, r_A is the receiving antenna's axial ratio in natural units and θ is the angle between the major axes of the polarization ellipses. We may fix θ such that we maximize the cosine for our worst-case analysis. We will fix the receiver antenna's axial ratio to 1 dB, independent from the look-angle. As for the antenna array in development, the axial ratio will depend on the implementation.

Figure 4.4 depicts the evolution of the polarization losses versus the axial ratio of the transmitter and various receiver axial ratios. Equation 4.7 gives negative values in dB to add to the link budget. The graph depicts its inverse, such that the values are positive. When both the receiver and the transmitter have identical axial ratios, we notice losses of 0 dB. For a receiver with perfect circular polarization, the polarization losses tend to 3 dB as the transmitter axial ratio increases. We notice losses increasing to 2.51 dB and 1.74 dB for a 1 dB and 3 dB axial ratio at the receiver, respectively. Having a 3 dB axial ratio at the receiver mitigates the polarization losses.

We can define the co-polarization (co-polar) directivity as the proportion of the total directivity contributing to the desired polarization. For perfect RHCP, if the

system has linear polarization, the co-polar directivity falls 3 dB below the total directivity [15]. We can connect this to the polarization loss assuming a perfect axial ratio at the reception, which leads to $|\rho_A|$ tending to infinity. In that case, we can develop Equation 4.7 as:

$$L_{pol}\ (\text{dB}) = 10\log_{10}\left(\frac{|\rho_W|^2}{(1+|\rho_W|^2)}\right) \tag{4.10}$$

Finally, the co-polar directivity is as:

$$D_{co-pol}\ (\text{dBi}) = D + 10\log_{10}\left(\frac{|\rho_W|^2}{(1+|\rho_W|^2)}\right) \tag{4.11}$$

4.3 System noise

As we are interested in the ratio between the signal and noise powers at the receiver to study the link feasibility, we must compute the system noise power. For that purpose, we will integrate the noise power spectral density, expressed in W/Hz, by the system bandwidth. Let us start by writing the noise power spectral density N_0 as:

$$N_0 = kT_s \tag{4.12}$$

In Equation 4.12, k is the Boltzmann's constant, and T_s is the complete system temperature. We now need to write the ratio between received power and noise power.

$$SNR = \frac{P_R}{N_0 B} = \frac{P_T G_T G_R}{kT_s B L_{trans}} \tag{4.13}$$

In Equation 4.13, L_{trans} is the total transmission losses, and B is the system bandwidth. We can expand the complete system temperature [11]:

$$T_s = T_{ant} + T_r \tag{4.14}$$

T_{ant} is the antenna temperature, which corresponds to the environment temperature seen by the system through the antenna radiation pattern. T_r is the equivalent noise temperature coming from the various circuit elements of the receiver connecting the antenna to the digital demodulator. The antenna temperature includes a dependence on the ground station elevation angle and frequency.

Table 3.1 contains the G_R/T_s ratio of the receiver. The latter is valid for an elevation angle of 20°. We can estimate its value for an elevation of 10°, which corresponds to the worst case. The ITU provides recommendations for brightness

Elevation	Temperature
10°	14 K
20°	8 K
30°	5.5 K
60°	3 K
90°	2.8 K

Table 4.1: Brightness temperature vs. ground station elevation angle.

temperature for various frequencies and elevation angles [16]. If the radiation pattern main beamwidth is narrow and encompasses a single noise source, the antenna temperature is equivalent to the brightness temperature. Table 4.1 gives the brightness temperature at 8 GHz for various ground station elevation angles. We can approximate the gain of a dish antenna by:

$$G = 0.7\frac{\pi^2 D^2}{\lambda^2} \tag{4.15}$$

D is the dish diameter in the last equation, and by inputting the problem data, we obtain a directivity of approximately 48.5 dBi. We fix the efficiency to 70%, which is standard for such antennas. It translates into a G_R/T_s ratio of 26.34 dB/K for an elevation of 10°.

4.4 Global link budget

Finally, we should gather the results to compute the total link budget. It is common to express it in dB. In that case, we write the SNR as:

$$\text{SNR (dB)} = P_T + G_T + \frac{G_R}{T_s} - kB - L_{FS} - L_{rain} + L_{pol} - M \tag{4.16}$$

We notice an additional term in the latter. M represents the additional margin we take for the link budget. Typically, we take a 3 dB margin. To compute the link budget, we will consider a transmitted power of 1 W. Note that we add L_{pol} as the definition given in Equation 4.7 gives negative values. As the radiation pattern and, more precisely, the axial ratio allows us to compute the polarization losses, we will group this quantity with the gain in transmit.

$$G_{T,eff} = G_T + L_{pol} \tag{4.17}$$

We define a new quantity, the effective gain in transmitting $G_{T,eff}$, corresponding to the radiation pattern's directivity, taking the polarization losses into account.

$G_{T,eff}$ dB	SNR dB	Bit per symbol
7.7	-2.4	0.5
11.2	1	1
16.8	6.68	2
18	7.88	2.2

Table 4.2: Achievable spectral efficiency for various antenna effective gains.

We can also name this quantity the effective directivity. We consider a 1 dB AR at the receiver. Table 4.2 gives the achievable bit rate for several effective gains. For a minimal SNR of -2.4 dB, we need a gain of 7.7 dB. The target gain of 18 dB will allow for transmitting 2.2 bits per sent symbol. In the worst case, the polarization losses are about 2.5 dB. Closing the link requires, in the worst case, a directivity of 10.2 dBi.

5 | Conformal antenna array

As the application targets a broad scanning range, we will investigate conformal antenna arrays, where the antenna arrays conform to a shape. This technique is appealing because the effective area of a planar array is proportional to the cosine of the elevation scan angle. Conformal arrays allow for boosting the antenna array effective area for more grazing angles. The drawback of such arrays is to have part of the antennas hidden behind the structure for particular scan-shape combinations. It is also worth noting that the beamforming weights are more challenging to optimize than in the planar array case and that the conformal nature of the system involves additional difficulties for the design and manufacturing process.

In Section 5.1, we will review the literature and present various state-of-the-art conformal array systems. We will select three geometries that may suit the application target. Section 5.2 presents the antenna placement on the three different shapes. To test-bench the different geometries, we coded a MATLAB software. We will describe this piece of software in Section 5.3. To improve the system directivity, we investigated different optimization strategies for the individual weights of the antenna elements. This investigation is the topic of Section 5.4. Finally, we will compare the different geometries in terms of performance in Section 5.5.

5.1 Literature review

We can find various geometries on which an antenna array can be conformed. We get a complete evaluation of the effective area for several shapes in Reference [17]. Based on the scanning objectives and the manufacturing complexity, we settled on a cone and a half-cylinder. This section will analyze both shapes, compare them with the planar array, and connect the discussion with the state-of-the-art literature.

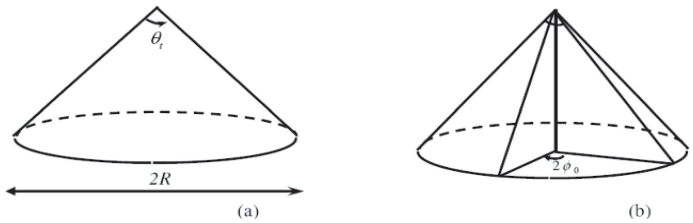

Figure 5.1: From [17]: Cone geometrical properties. (a) Cone apex angle and diameter. (b) azimuthal width of the active area $2\phi_0$.

5.1.1 Cone

The cone has the advantages of being symmetric and will provide a constant effective area for an azimuthal scan. Let us write its effective area as in Reference [17]:

$$\cos(\phi_0) = \frac{\cos(\theta_{max} - \theta_s \sin(\theta_t/2))}{\sin(\theta_s)\cos(\theta_t/2)} \tag{5.1}$$

$$A_{eff} = R^2 \left(\frac{\sin(\theta_s)\sin(\phi_0)}{\tan(\theta_t/2)} + \phi_0 \cos(\theta_s) \right) \tag{5.2}$$

Figure 5.1 gives a representation of the cone parameters. The effective area depends on the cone radius R, the cone apex angle θ_t, maximum element look angle θ_{max} (equivalent to the element radiation pattern beamwidth), and the elevation scan angle θ_s. From Equation 5.2, we note that the effective area decreases as the scan angle increases.

Reference [18] presents a cylindrical-and-conical conformal phased array (CYL-CON). Figure 5.2 gives a representation of this structure. It has three distinctive arrays: a conical array and two cylindrical arrays. Array I is a conically conformed microstrip antenna array designed for achieving forward beam coverage. Array II is a cylindrically conformed microstrip antenna array designed for achieving broadside beam coverage. Finally, array III is a cylindrically conformed microstrip Yagi antenna array designed to achieve backward beam coverage. Thanks to these three different arrays, the system offers a broad scanning range.

Figure 5.3 presents the directivity of the conically conformed microstrip antenna array in the YZ plane. As the prototype array does not cover the whole cone azimuthal width, the directivity is the highest when the observer faces the elements. When the array covers the whole azimuthal width, the directivity is the highest at the zenith as the cone hides no antenna and more antennas are in the line of sight with the observer.

Figure 5.4 presents the directivity of the cylindrically conformed microstrip antenna array in the YZ plane. Like for the planar antenna array, the directivity

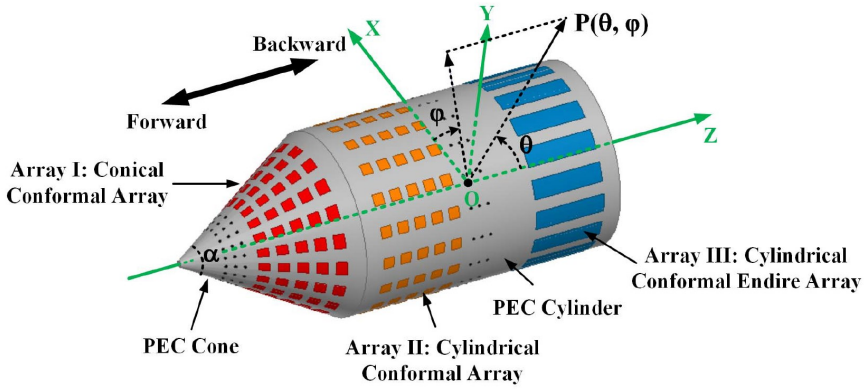

Figure 5.2: From [18]: Representation of the CYLCON conformal arrays composed of a conically conformed microstrip antenna array (Array I), a cylindrically conformed microstrip antenna array (Array II), and a cylindrically conformed microstrip Yagi antenna array (Array III).

decreases as the cosine of the elevation scan angle in that plane. That angle corresponds here to $90° - \theta$. We notice a decrease of about 3 dB between the curves $\theta = 30°$ and $\theta = 90°$, which corresponds to $\cos(60°)$.

5.1.2 Half-cylinder

The half-cylinder will offer a broad elevation scan if the direction of observation is perpendicular to the half-cylinder height, meaning that the observer faces the shape curved surface. We obtain the effective area by projecting the shape surface onto the plane perpendicular to the propagation direction (cf. Figure 5.5b). The effective area of the cylinder depends on the cylinder radius R, the cylinder height h, and the active sector Δ_ϕ defined in Figure 5.5a. We can write it as [17]:

$$A_{eff} = 2Rh \sin\left(\frac{\Delta_\phi}{2}\right) \tag{5.3}$$

It decreases as the active sector decreases. For a half-cylinder, Δ_ϕ varies from π to $\frac{\pi}{2}$. It thus does not go to zero as the elevation angle goes to $\frac{\pi}{2}$. Still, it suffers from having hidden elements for certain scan angles, which leads to a decrease in the active sector. If the observer faces one of the flat surfaces, on the contrary, the effective area will also vary as the cosine of the elevation, and the performance will degrade for grazing angles. In between those two extremes, we have a hybrid situation where we experience both effects.

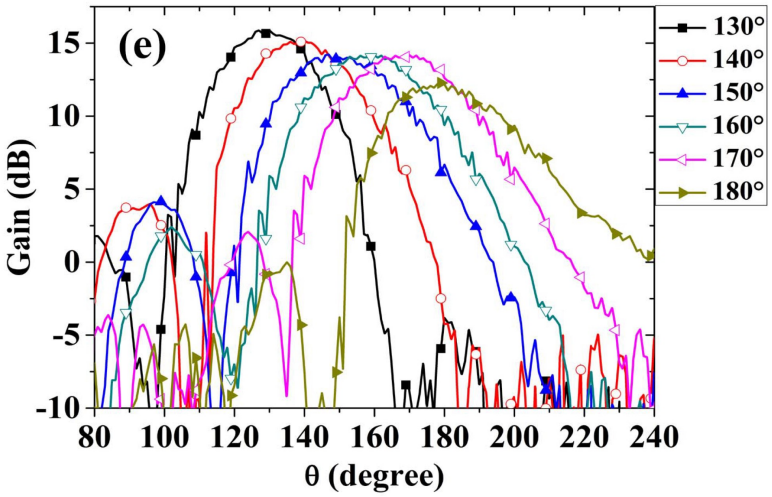

Figure 5.3: From [18]: Directivity of the conically conformed microstrip antenna array in the YZ plane for various elevation scan angles.

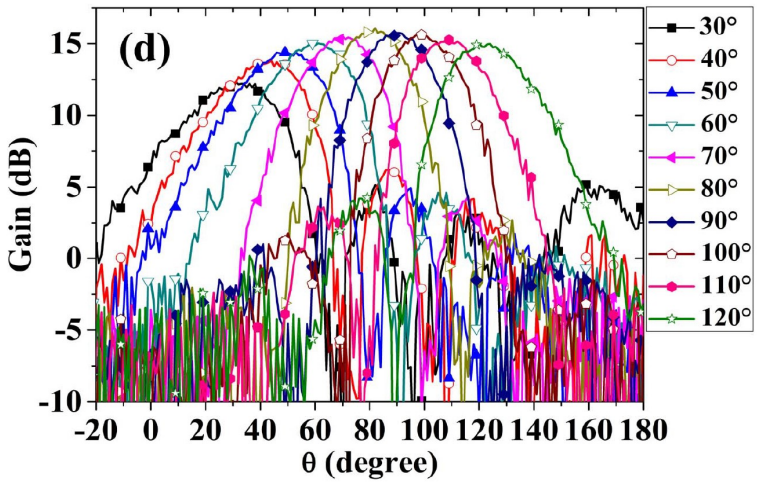

Figure 5.4: From [18]: Directivity of the cylindrically conformed microstrip antenna array in the YZ plane for various elevation scan angles.

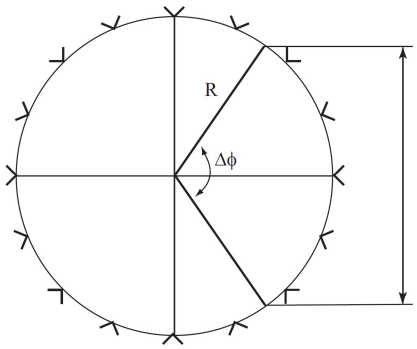

(a) Cylinder active sector Δ_ϕ definition.

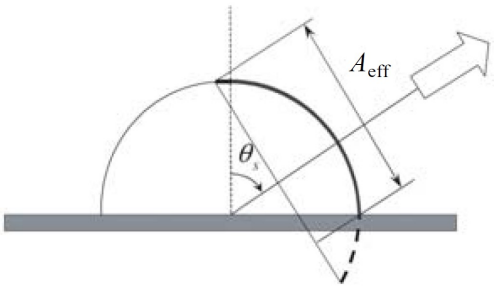

(b) The half-cylinder effective area, obtained by projecting the shape surface onto the plane perpendicular to the direction of propagation.

Figure 5.5: From [17]: Cylinder properties.

Reference [19] proposes a Cylindrical Phased Array (CPA) allowing quasi-full-space scanning thanks to the pattern reconfigurable technique with a subarray scanning method. The reconfigurable pattern technique consists of modifying the antenna elements' radiation pattern using a specific bias of the PIN switch diodes present in the elements. This technique improves the scanning in the azimuthal plane (parallel with the cone height), reaching a range of $\pm 70°$ for the main beam and a 3-dB coverage of $\pm 88°$. The CPA offers a complete scanning in the elevation plane (perpendicular with the cone height) thanks to the alignment of the elements with the direction of observation. Figure 5.6 represents both the scanning resolution and a prototype of the system, composed of six facets.

5.2 Antennas placement

This section will describe the placement of the different antenna elements over three different shapes: a planar surface, a cone, and a half-cylinder. As we target a high gain, we will try to fit as many elements as possible on the shapes. The different geometries need to satisfy the system maximum physical size given in Table 3.1. We usually target a half-wavelength distance between the successive antennas to lower the level of the radiation pattern side lobes. That is close to 18.3 mm at 8.2 GHz. Considering faceted shapes allows the design of planar antennas and makes it easier to build and feed such structures. It may also allow designing only one facet and replicating it to build the whole structure finally. In the following figures, we represent each antenna by a color dot.

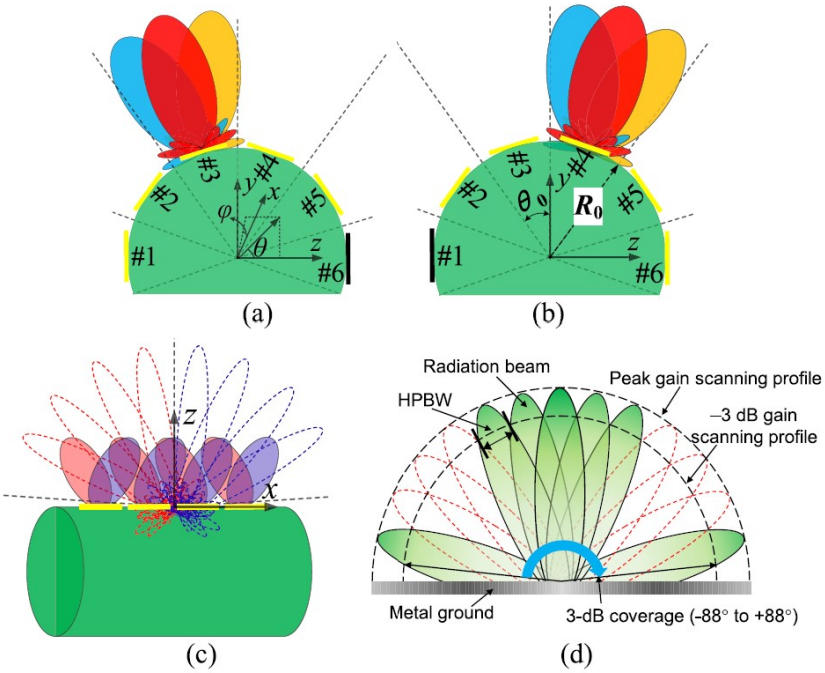

(a) - (a) and (b) Scanning resolution in the third and fourth sectors of the cylindrical carrier's azimuth plane. (c) Elevation plane patterns of the cylindrical carrier when all the elements are active with the correct configurable patterns. (d) Sketch diagram of the 3 dB coverage.

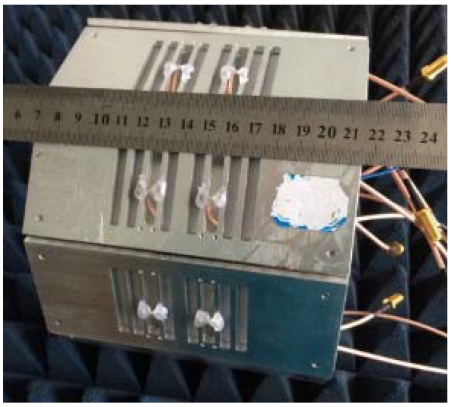

(b) Prototype of the proposed architecture. Half-cylinder made of 6 facets.

Figure 5.6: From [19]: CPA scanning space division illustration and prototype of the proposed architecture.

Figure 5.7 depicts the placement of the antennas on the conical conformal antenna array. The cone has an apex angle of 80°, a radius of 7.5 cm, and contains three rings of 16 elements for a total of 48 antennas. The distance between the rings along the generatrix is half-wavelength. Within the top ring, the distance between the elements is close to a half-wavelength. For the two lower rings, the distance is more significant than that due to the cone geometry.

Figure 5.8 depicts the placement of the antennas on the half-cylindrical conformal antenna array. The half-cylinder has a radius close to 4 cm and a height of 15 cm. Within the rows, the elements have a half-wavelength distance between them. Because of the angle between two rows on the half-cylinder surface being $\pi/7$ and because of the half-cylinder radius, we obtain a separation of a half-wavelength between two rows. We place two extra 2×2 arrays on the cylinder's flat surfaces with a half-wavelength distance between the elements. Those small extra arrays will boost the directivity for specific azimuthal angles. As we have seven rows of eight elements each plus two arrays of four elements each, the system has a total of 64 antennas.

Figure 5.9 depicts the placement of the antennas on the planar array. We separate the elements by a half-wavelength in both the x and y dimensions. The array is an 8×8 array composed of 64 elements in total.

At this stage, we can point out that both the planar and cylindrical arrays have the same number of elements. That is not the case with the conical array. We still want to compare the three and are aware that it will mitigate the performance of the conical array. However, because the specifications restrict the geometry of the array and that we want to standardize the facets composing the cone, we had to limit the number of antennas. In practice, if we were to build such a structure, we would care about this aspect. That is why we are dealing with a reduced number of antennas for the conical array.

5.3 Test-bench description

To properly compare the different topologies, we had to build a test bench. For doing so, we wrote a MATLAB software. We designed a simple X-band antenna using CST STUDIO SUITE by 3ds (CST) to get an accurate far-field radiation pattern for the computations. Figure 5.10 gives the antenna directivity and axial ratio. The software will place the antennas with the proper orientation as depicted in Section 5.2. It will then sum the different radiation patterns to measure the equivalent radiation pattern for specific antenna weights. Note that we do not include the effects of coupling between the antennas. Placing the antennas in an array will modify their radiation patterns. We talk about the embedded pattern of the antenna, that is, the pattern of one antenna in the presence of the other

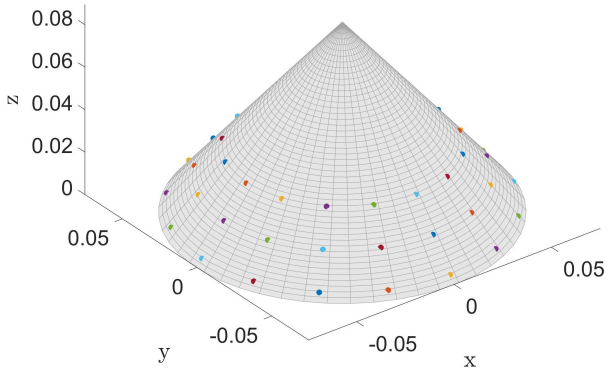

(a) Placement of the antennas on the conical conformal antenna array. The cone has an apex angle of 80° and a radius of 7.5 cm.

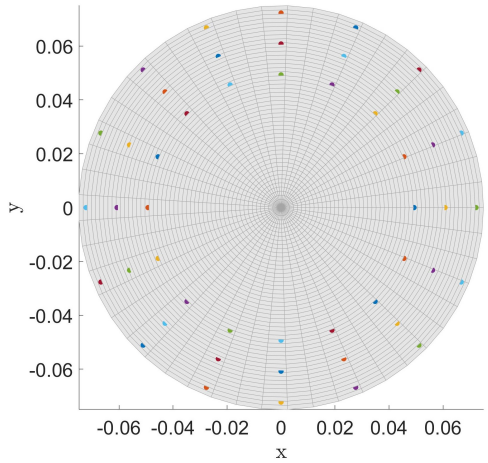

(b) Top view: Placement of the antennas on the conical conformal antenna array. It contains three rings of 16 elements for a total of 48 antennas. The distance between the rings along the generatrix is half-wavelength. Within the top ring, the distance between the elements is close to a half-wavelength.

Figure 5.7: Placement of the antennas on the conical conformal antenna array.

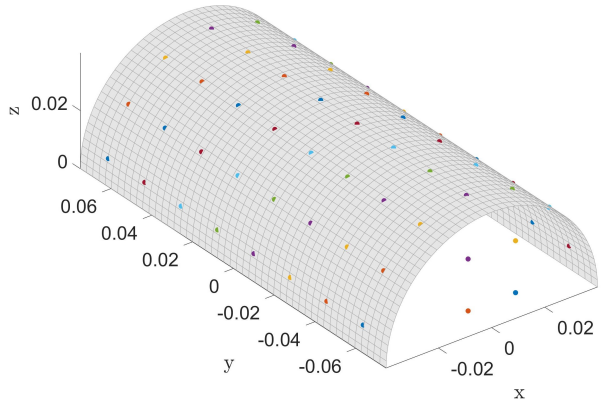

(a) Placement of the antennas on the half-cylindrical conformal antenna array. The half-cylinder has a radius close to 4cm and a height of 15 cm. Within the rows, the elements have a half-wavelength distance between them.

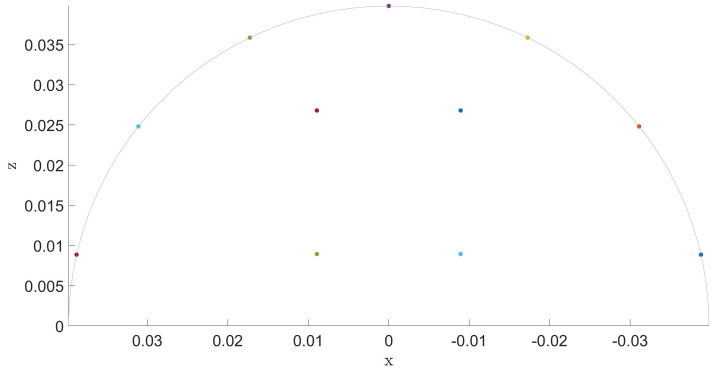

(b) Side view: Placement of the antennas on the half-cylindrical conformal antenna array. The angle between two rows on the cone surface is $\pi/7$ to obtain a separation of a half-wavelength between two rows. We place two extra 2×2 arrays on the cylinder's flat surfaces with a half-wavelength distance between the elements.

Figure 5.8: Placement of the antennas on the half-cylindrical conformal antenna array.

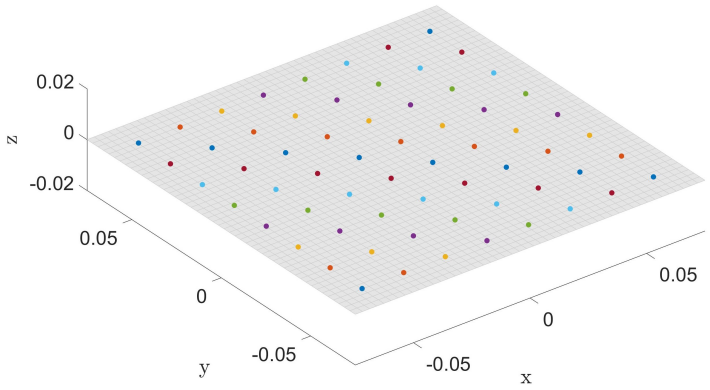

Figure 5.9: Placement of the antennas on the planar array. We separate the elements by a half-wavelength in both the x and y dimensions.

antennas of the array. Still, as the elements are spaced by a half-wavelength, not taking the coupling effects into account is a valid first approximation. We must then compute the directivity and axial ratio of the pattern in the direction of observation. Those two figures of merit will characterize the performance of the system. It is also essential to measure the amplitudes of the coefficients as those will dictate the transmitted power. Finally, we can perform an optimization of the different phases and amplitudes to improve the directivity.

5.4 Weight optimization applied to conformal arrays

The weight optimization for a conformal array is more challenging than for a planar array. As the problem is complex and has numerous local optimums, choosing a proper initial vector is critical. We developed two possible initial vectors. The first one only corrects the phase, where the second also tunes the amplitude of the elements. We finally compare the two and showcase the possible improvement from using MATLAB's implementation of the interior-point algorithm on top of these initial vectors.

5.4.1 Phase compensation

Applying the proper weights to the array's antennas allows scanning a beam, as presented in Section 2.7. In Equation 2.27, we developed the radiation pattern as the sum of the different contributions. We can put the antenna element radiation pattern in evidence for a planar array as all the antennas have the same orientation.

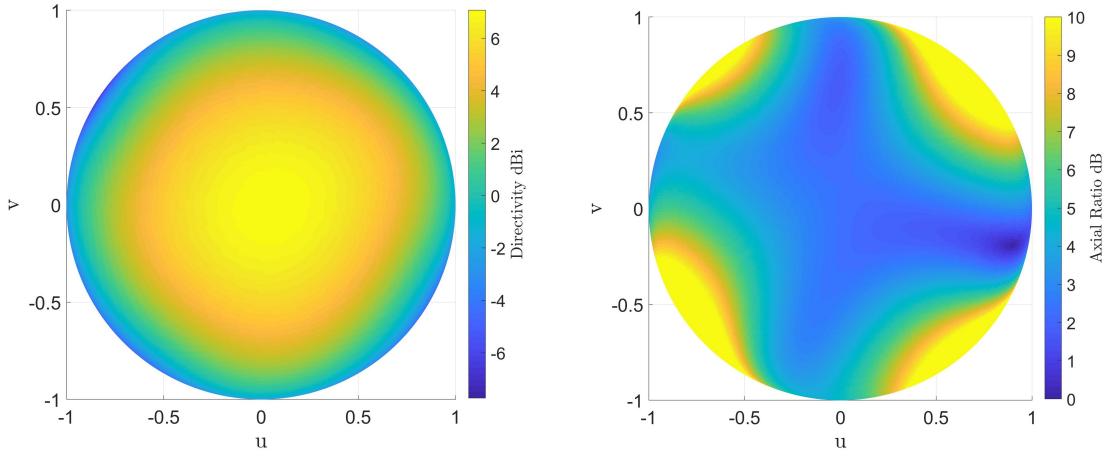

(a) Antenna directivity.

(b) Antenna axial ratio. Upper bounded at 10 dB.

Figure 5.10: Far-field radiation pattern characteristics of the X-band antenna used by the MATLAB software.

In all generality, we can re-write that equation as:

$$\mathbf{F}(\mathbf{u}) = \sum_n \mathbf{F}_0(\mathbf{u}_n)\alpha_n e^{j\beta_n} e^{jk\rho_n \cdot \mathbf{u}} \tag{5.4}$$

The element radiation pattern is inside the sum in Equation 5.4, and the direction of observation varies with the selected element. Indeed, when dealing with a conformal array, the antennas have different orientations. It involves an additional challenge as we must compute the phase shift introduced by each antenna to compensate for it. We do not include coupling effects in the test bench and use the element radiation pattern knowledge to obtain perfect phase compensation. In practice, it involves measuring the embedded pattern for every antenna.

$$\mathbf{F}(\mathbf{u}) = \sum_n (E_\theta(\mathbf{u}_n)e^{je_\theta(\mathbf{u}_n)}\hat{\theta} + E_\phi(\mathbf{u}_n)e^{je_\phi(\mathbf{u}_n)}\hat{\phi})\alpha_n e^{j\beta_n} e^{jk\rho_n \cdot \mathbf{u}} \tag{5.5}$$

In Equation 5.5, E_θ (E_ϕ) is the magnitude of the field's theta (phi) component, and e_θ (e_ϕ), its phase. To compensate for this phase shift, we must set β_n as:

$$\beta_n = k\rho_n \cdot \mathbf{u} + e_\theta(\mathbf{u}_n) \tag{5.6}$$

Due to the geometry of the array, the shape may hide some antennas for specific scan angles. Enabling these antennas would spill energy in non-desired directions, decreasing the directivity. That is why we disable these antennas when not in the observer's line of sight. For the other antennas, we use a constant amplitude.

5.4.2 Amplitude normalization

Using a phase compensation technique with constant amplitudes may be sub-optimal when dealing with conformal arrays. Indeed, a conformal array allows for different orientations of the antennas on the structure. As the antenna radiation pattern is more directive towards the broadside, we could feed more power to the elements facing the scan direction more closely than the other elements. To formalize this intuition, we can fix the radiation pattern magnitude's weights amplitude at the scan direction normalized to its maximum. Note that the amplitude is upper bounded not to saturate the amplifiers.

$$\alpha_n = \frac{\sqrt{|F_{n,\theta}(\mathbf{u}_n)|^2 + |F_{n,\phi}(\mathbf{u}_n)|}^2}{\max\left(\sqrt{|F_{n,\theta}(\mathbf{u}_n)|^2 + |F_{n,\phi}(\mathbf{u}_n)|^2}\right)} \tag{5.7}$$

5.4.3 Comparison and further improvement

We can further improve the system directivity by optimizing the initial weights. For that, we use the MATLAB implementation of the interior-point algorithm. We decided to optimize the directivity taking the polarization losses into account. To test the different procedures, we apply them to the half-cylinder geometry introduced in Section 5.2. We scan a beam for increasing elevation in the $\phi = 0°$ plane (facing the half-cylinder curved surface), and we distinguish serval cases for the weights:

- Phase compensation with no additional optimization.
- Phase compensation with phase optimization (5 iterations).
- Phase compensation and amplitude normalization with no additional optimization.
- Phase compensation and amplitude normalization with phase optimization (5 iterations).
- Phase compensation and amplitude normalization with joint phase and amplitude optimization (5 iterations).

Figure 5.11 gives the directivity for these five cases. We notice that modifying the amplitudes of the different elements of the arrays allows for improving the directivity. We notice peaks in directivity when the elevation angle is a multiple of $\pi/7$, when the observer faces a row of antenna. That effect is enhanced when we perform amplitude normalization as it increases the relative power fed to those antennas.

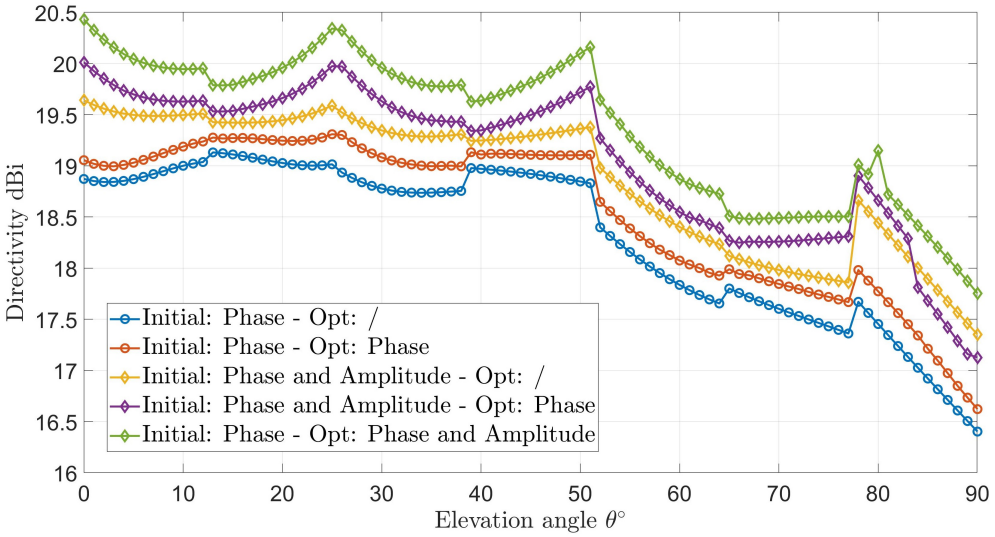

Figure 5.11: Directivity comparison for the half-cylinder in the $\phi = 0°$ plane between the two initial vectors and various optimizations.

As the elevation angle increases, the directivity decreases as fewer antennas are in sight with the observer, and the structure hides some.

The drawback of the amplitude normalization is that reducing the amplitudes of some coefficients will decrease the system transmit power. That is because the amplifiers will saturate, which fixes an upper bound for the amplitudes. That implies decreasing the system power instead of keeping it constant and redistributing it. The total available power is the sum of the power fed to the different antennas:

$$P_{tot} = \sum_n P_n \tag{5.8}$$

$$= \sum_n P_0 \alpha_n^2 \tag{5.9}$$

$$= P_0 \sum_n \alpha_n^2 \tag{5.10}$$

In Equations 5.8 to 5.10, P_{tot} is the total Transmitter (TX) power, and P_0 is the element nominal TX power. Let us now compare the total system power with its maximum power.

$$\frac{P_{tot}}{P_{max}} = \frac{P_0 \sum_n \alpha_n^2}{P_0 N_{ant}} \tag{5.11}$$

$$\frac{P_{tot}}{P_{max}} \text{ dB} = 10 \log_{10}(\sum_n \alpha_n^2) - 10 \log_{10}(N_{ant}) \text{ dB} \tag{5.12}$$

Equation 5.12 gives the expression of the power loss due to the coefficient reduced amplitudes. In these equations, N_{ant} is the system total number of antennas. Figure

5.12 compares the two initial vectors (phase compensation only; phase compensation and amplitude normalization) with the additional effect of power normalization. We notice that modifying the amplitudes will decrease the performance even if it gives better directivity than the initial vector using the phase compensation technique. We also notice a power loss coming from the switched-off antennas hidden by the structure.

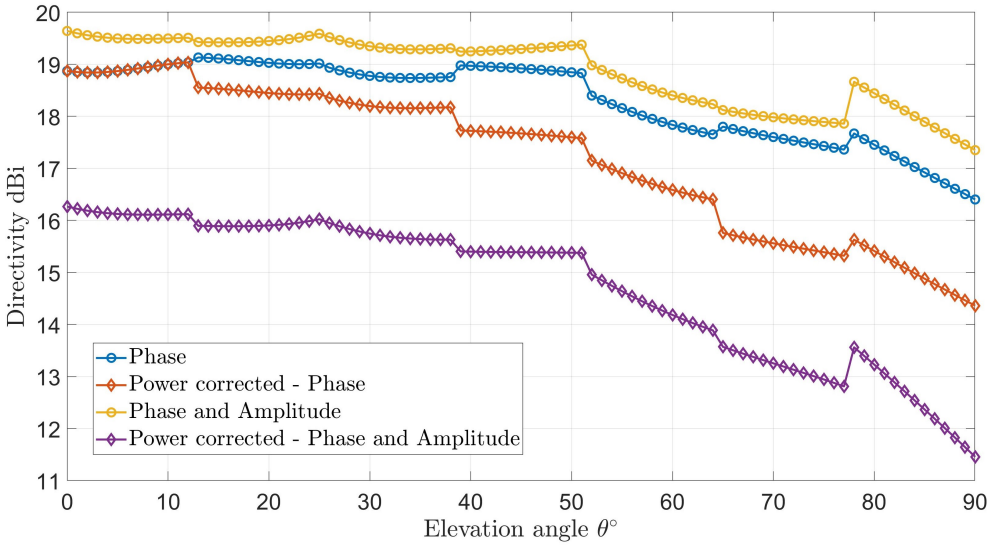

Figure 5.12: Directivity comparison for the half-cylinder in the $\phi = 0°$ plane between the two initial vectors, including power normalization correction.

5.5 Shape comparison and selection

We need to rank the shapes introduced in Section 5.2 and select one of them for the application. For that, we compare the directivity for the entire scan range with a one-degree precision. We also take the polarization losses and the power normalization losses into account. We will use only the phase compensation technique for each shape as we saw in the previous section that modifying the weights amplitudes decrease overall performance. We will not perform any additional optimization since the performance increase is limited compared to the required computation time. Let us now define the total transmitter gain as:

$$G_{t,tot}\ \text{dB} = G_t + L_{pol} + \frac{P_{tot}}{P_{max}}\ \text{dB} \tag{5.13}$$

That expression takes the polarization losses and power normalization losses into account.

5.5.1 Planar array

Figure 5.13 depicts both the directivity and total transmitter gain for the 64 elements planar array using only the phase compensation technique to compute the beamforming weights. It gives a small variation in the azimuthal scan. Since all the elements have unit amplitude, and no element is hidden, the total gain only suffers from the polarization losses. Indeed, between Figure 5.13a and Figure 5.13b, we notice only a tiny gain variation.

5.5.2 Conical conformal array

Figure 5.14 depicts both the directivity and total transmitter gain for the 48 elements conical conformal array using only the phase compensation technique to compute the beamforming weights. We note a slight variation in the azimuthal scan. In this case, we notice significant differences between the directivity and the total gain. We normalize the power to 64 elements to compare the system to the two others better. It is challenging to place 64 antennas on a cone of this size, so we only have 48 antennas. As mentioned previously, we want to propose a relatively easy-to-build conformal array. The conformal array also suffers from the hidden antennas for high elevation angles, adding extra power losses. These hidden antennas cause the discretization effect for the total gain. Indeed, antennas remain visible for a specific scan range, then some become hidden, and the gain drops.

5.5.3 Half-cylindrical conformal array

Figure 5.15 depicts both the directivity and total transmitter gain for the 64 elements half-cylindrical conformal array using only the phase compensation technique to compute the beamforming weights. We note the substantial variation in the azimuthal scan. That is because of the shape itself, non-symmetric along ϕ. We also notice the power losses coming from the hidden and disabled antennas.

5.5.4 Shape comparison

Finally, we can compare the three different shapes and make a selection. Figure 5.16 compares their best and worst directivity, Figure 5.17, their best and worst total transmitter gain along the azimuthal angle ϕ. The use of conformal arrays allows boosting the directivity for high elevation angles that are not of interest to this application. Indeed, we target elevation angles $\theta \leq 65°$. In addition to that, the power loss coming from the hidden and disabled antennas further reduces the conformal array performance for the scanning range of interest. The minimal

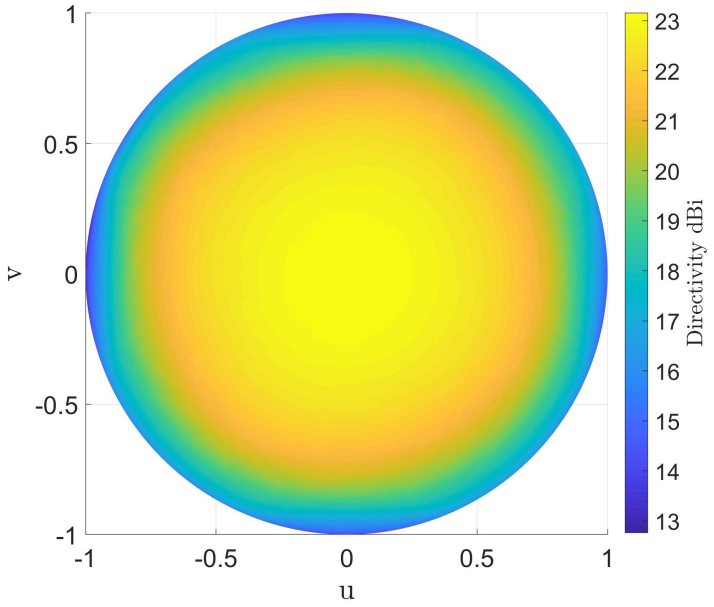

(a) Full scan directivity in dBi.

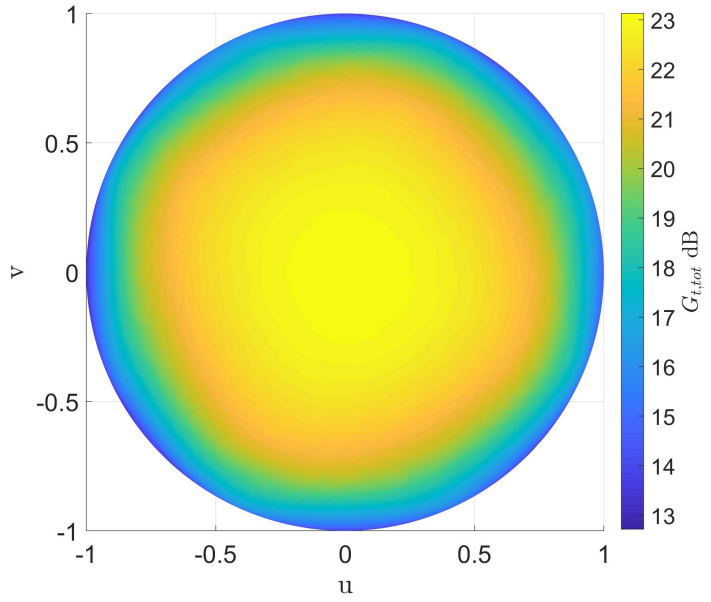

(b) Full scan total transmitter gain in dB.

Figure 5.13: Full scan results for the 64 elements planar array using only the phase compensation technique.

total gain for the planar array outperforms the maximal total gain for the half-cylinder for elevation angles $\theta \leq 60°$. Furthermore, the planar array is less complex

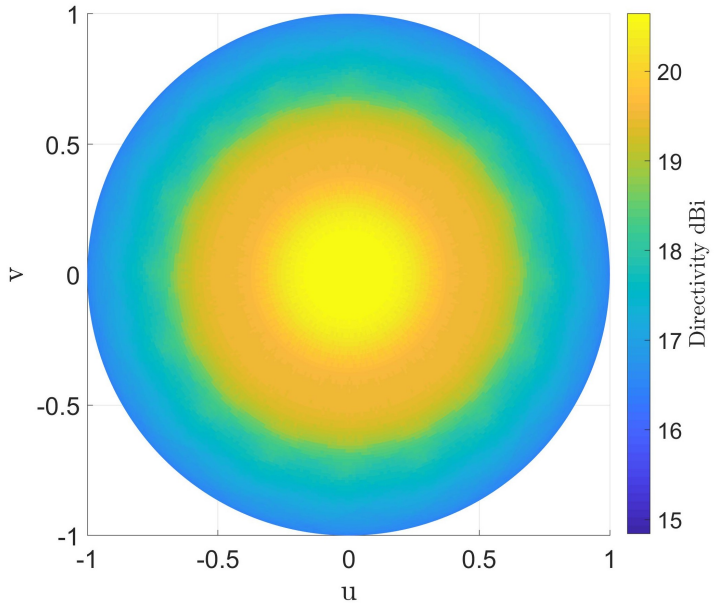

(a) Full scan directivity in dBi.

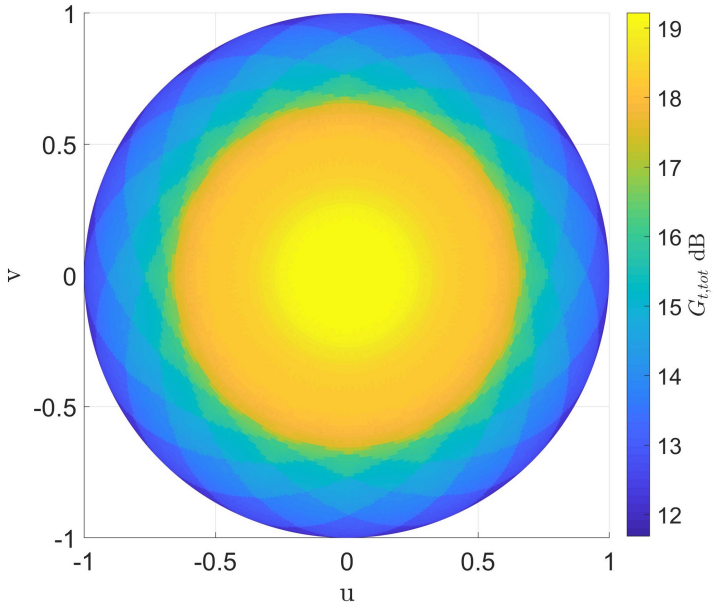

(b) Full scan total transmitter gain in dB normalized to 64 elements.

Figure 5.14: Full scan results for the 48 elements conical conformal array using only the phase compensation technique.

to manufacture. For these reasons, we select the planar antenna array for the remaining chapters.

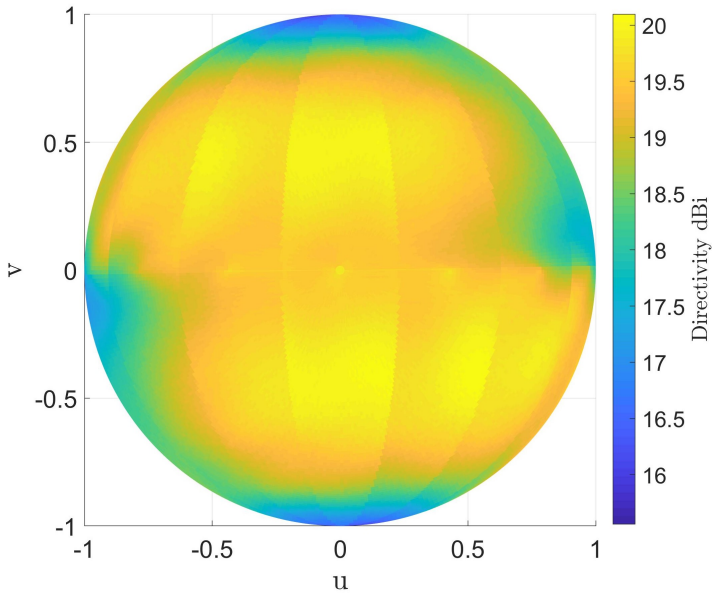

(a) Full scan directivity in dBi.

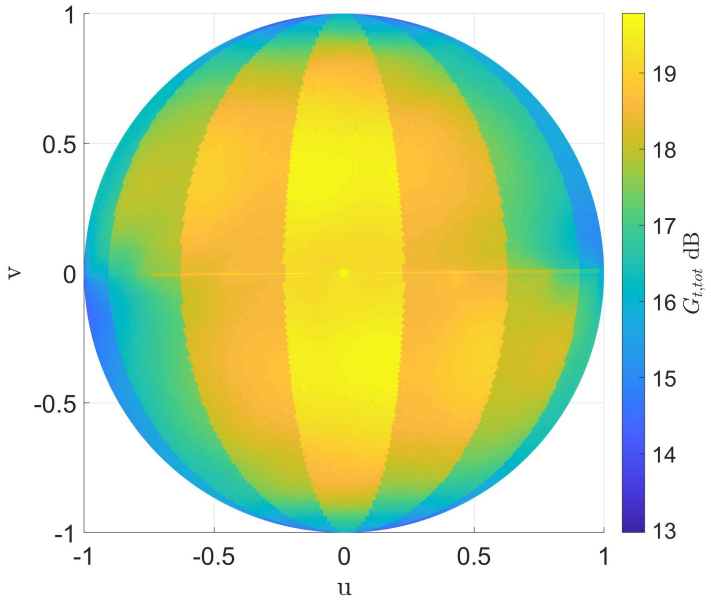

(b) Full scan total transmitter gain in dB.

Figure 5.15: Full scan results for the 64 elements half-cylindrical conformal array using only the phase compensation technique.

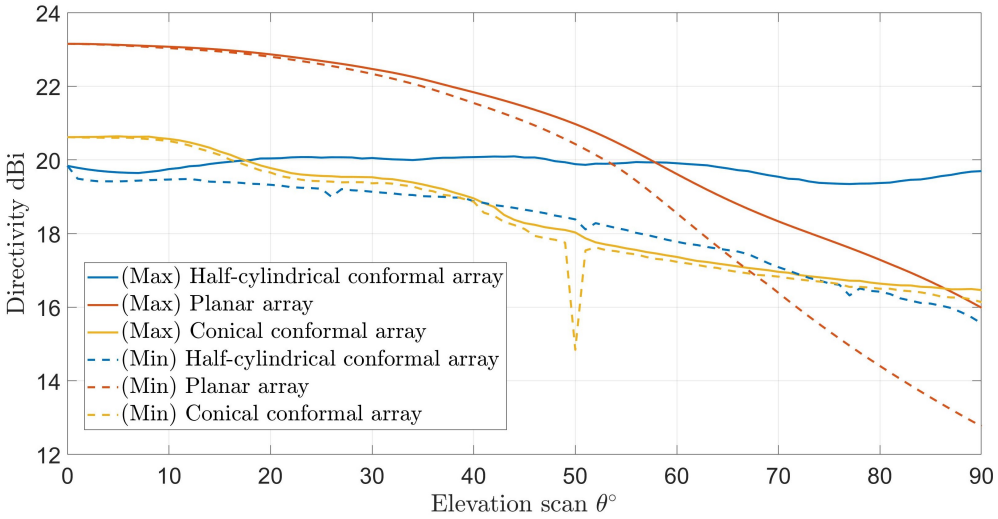

Figure 5.16: Best and worst case directivity comparison along with the azimuthal angle ϕ versus the elevation angle.

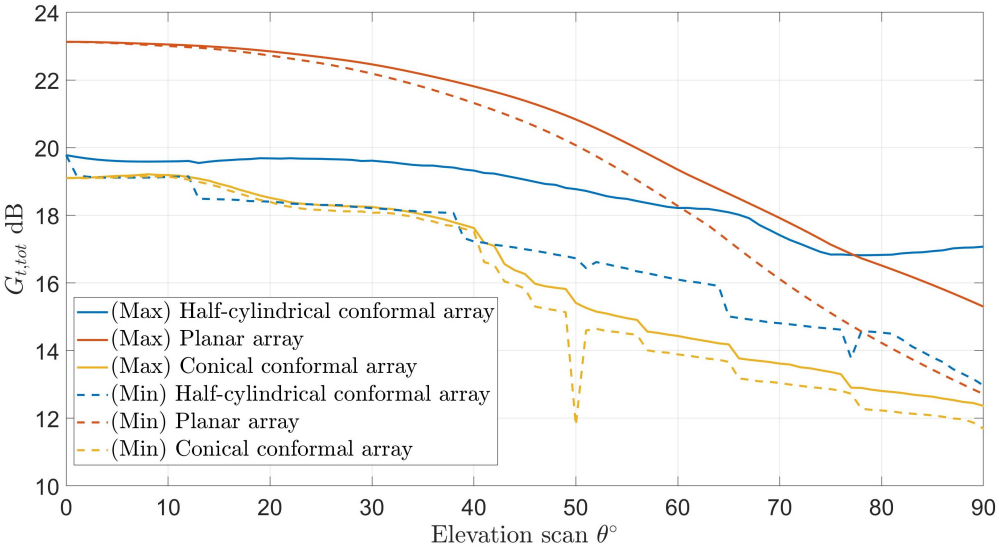

Figure 5.17: Best and worst case total transmitter gain comparison along with the azimuthal angle ϕ versus the elevation angle.

6 | Beamforming network

This chapter will focus on the system beamforming network. To properly feed the antennas, we must use devices to modify the phase and amplitude of the incoming Radio Frequency (RF) signal. Those devices are beamformers. We also need power dividers to feed the RF signal among them.

First, Section 6.1 will introduce a potential RF transmitter chain and define the parts and components present on the antenna board. In Section 6.2, we pick several beamformers references and compare them to several criteria. We will also present a selection for the power dividers. Section 6.3 gives a non-exhaustive list of considerations for the system layout. Finally, Section 6.4 gives a first layout proposal.

6.1 Communication chain

Figure 6.1 gives the block diagram of a radio frequency transmitter. First, the modulator modulates the incoming data according to the modulation scheme of choice. We then filter this signal using an intermediate frequency filter. Next, a mixer mixes the signal to a frequency set by the local oscillator. Then, a bandpass filter filters the signal and mitigates the signal power outside the application band. Power dividers will then split this RF signal and feed it to the different beamformers, modifying the signal phase and amplitude to feed it to the antennas finally. The power dividers, beamformers, and antennas will be onboard. The board will have an RF connector connecting the bandpass filter output to the circuit.

6.2 Chip selection

This section focuses on selecting the onboard circuit components: the power dividers and the beamformers.

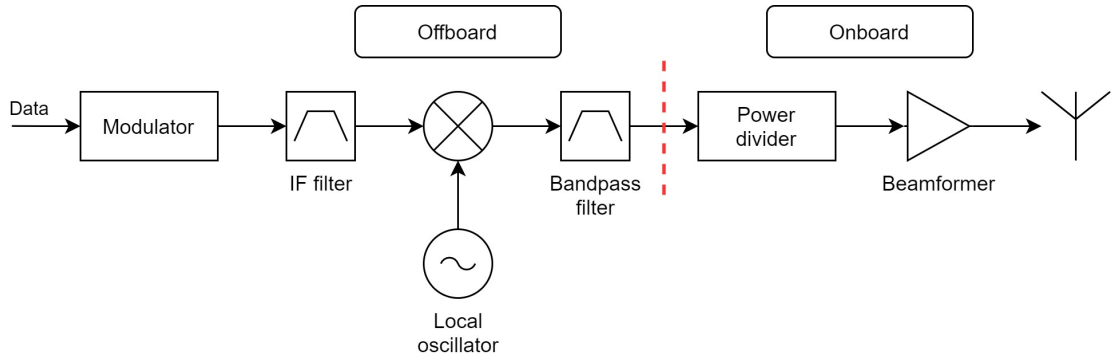

Figure 6.1: Block diagram of the RF transmitter. The power dividers, beamformers, and antennas will be onboard. The board will have an RF connector connecting the bandpass filter output to the circuit.

6.2.1 Beamformers

The chip selection implies looking into the manufacturers' catalogs to find suitable references. We target digital beamformers with a high level of integration and control. We use several criteria to perform this selection:

- Suitable for spatial applications: The chip needs to resist cosmic radiation and large temperature gradients.
- Operating frequency: The chip needs to be functional on the application band (8025-8400 MHz).
- Power consumption: The chip efficiency and the overall system power consumption is critical as the system works on rechargeable batteries.
- The number of RF TX ports: 64 should be a multiple of the chip's number of ports. Numerous ports and a high level of integration also reduce the DC power overhead.
- Phase resolution: It impacts the precision of the phase compensation, and thus, the scan precision.
- One dB compression point: It fixes the maximum TX power of the antennas and thus of the system. In practice, we do not use the amplifier at that level of power to avoid saturation. Still, it gives an upper bound for the transmit power.
- Package dimensions: the chip package should have sub-wavelength dimensions.

Table 6.1 gives the three chips selection based on those criteria. All are suitable for spatial applications. The Anokiwave beamformer's datasheet mentions operating frequencies higher than the application band. According to the manufacturer, the chip can handle the application band. The phase resolution offered by all devices is sufficient. The directivity loss is well below 0.1 dBi. The ADAR1000 and the AWS-0101 support four ports, which is helpful to feed the 64 elements. That gives a total of 16 beamformers.

We notice a higher one dB compression point for the AWS-0101 than for the ADAR1000. That metric will fix the chip's output RF power, and thus, the total TX power. We can translate the power in Watt using Equation 6.1. The CGY2170YUH requires a consequent RF power input compared to the other two, challenging to carry. The ratio between the total RF and total DC power indicates the chip's efficiency. The AWS-0101, with its high level of integration, gives better efficiency than the ADAR1000. It also offers the highest RF output power.

For those reasons, the AWS-0101 stands out from the competition. The ADAR1000 remains a decent alternative. We discard the CGY2170YUH due to its number of ports and low TX gain requiring a high RF input power.

$$P\ [\mathrm{W}] = 10^{(P\ [\mathrm{dBm}]-30)/10} \tag{6.1}$$

6.2.2 Power dividers

We choose Wilkinson power dividers for our application. The input power will split into two output channels. By putting several power dividers in series, we will end up with 16 balanced channels to connect to the beamformers. For our selection, we can again select a few suitable references and compare them. We use the following criteria for this comparison:

- Suitable for spatial applications: The chip needs to resist cosmic radiation and large temperature gradients.
- Operating frequency: The divider must be functional on the application band (8025-8400 MHz).
- Amplitude and phase balance: The divider needs to avoid creating phase or amplitude unbalance between the two channels.
- Excess insertion loss: We have several dividers in series and require a low excess loss to maintain the input power low. The excess insertion loss is the common port to output port insertion loss minus 3 dB.

Parameter	Unit	Chips		
Reference	-	ADAR1000	CGY2170YUH	AWS-0101
Reference Brand	-	Analog Devices	Ommic	Anokiwave
Operating frequency	GHz	8-16	8-12	8.5–10.55
Phase resolution	°	2.8 (7 bits)	5.625 (6 bits)	5.625 (6 bits)
Number of RF ports	-	4	3	4
Package dimensions	mm x mm	7x7	4.7x3.8	7x7
Channel TX gain	dB	20	6	20
Channel P1dB	dBm	9	11	13
Chip RF input power	mW	0.317	9.486	0.798
Chip RF output power	W	0.032	0.038	0.079
Total RF input power	W	0.005	0.202	0.012
Total RF output power	W	0.508	0.806	1.277
Chip DC power	W	1.4 (est.)	0.36	1.8
Total DC power	W	22.4	7.92	28.8
RF/DC Power	%	2.26	10.17	4.43

Table 6.1: Beamformers comparison table.

- Package dimensions: The divider package should have sub-wavelength dimensions.
- Power as a divider: The divider must withstand enough power to supply the beamformers plus a safety margin to carry the losses.

Table 6.2 gives a comparison between three dividers from the brand Marki microwave. We select the PD-0530SMG as it has the best phase and amplitude balance, the best output to output isolation, and a well-sized package. We could also select the PD-0535SM. On the other hand, the package size of the PD-0434SM is larger and thus more challenging to deal with than the two other dividers.

To get 16 channels from one, we require 15 power dividers. To get similar amplitude at each beamformer's input, we will connect them such as we have four dividers in series for each channel. The system has an additional power loss of 6 dB in this configuration, which roughly translates into a factor of one over four. The input power needs to be four times larger than the total RF input power written in Table 6.1.

Parameter	Unit	Power dividers		
Reference	-	PD-0530SMG	PD-0434SM	PD-0535SM
Reference Brand	-	Marki microwave		
Operating frequency	GHz	5-30	4-34	5-35
Amplitude Balance	dB	±0.1	±0.25	±0.25
Phase Balance	°	±2	±3	±3
Excess Insertion Loss	dB	1.5	1.5	1.5
Output to Output Isolation	dB	25	20	18
Power As Divider	W	10	10	10
Package dimensions	mm x mm	6.1 x 3.81	11.43 x 3.81	6.1 x 3.81

Table 6.2: Power dividers comparison table.

6.2.3 Chip selection summary

We choose the AWS-0101 from Anokiwave for the beamformers and the PD-0530SMG from Marki microwave for the power dividers. The system requires a total input RF power of 0.048 W and a total DC supply power of 28.8 W. Note that extra losses from the propagation of the waves into the feeding lines will increase the RF input power requirement.

The beamformer has a P1dB of 13 dBm. That translates into a total RF output power of 1.277 W at most. In practice, we do not operate at the P1dB and take some margins to avoid saturation. Furthermore, the antennas have a radiation efficiency of less than 100%, implying additional losses.

6.3 Layout considerations

When considering the placement of the different elements on a board, we need to study several aspects carefully. We give a non-exhaustive list of important considerations.

6.3.1 Multi-layer PCB stack-up

The beamformers require multiple inputs to function correctly: power supply, ground, RF input, control. That motivates the use of a multi-layer Printed Circuit Board (PCB) stack-up. Indeed, depending on the integrated circuit of choice, we may dedicate layers to carry the power signals, the ground, and the control. Reference [20] presents a multi-layer PCB stack-up with ten metal layers and a dedicated layer for the SPI control. Reference [21] showcases a stack-up with 14

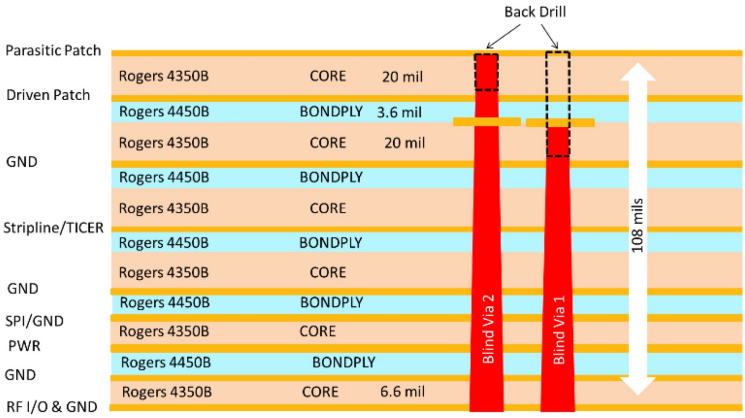

Figure 6.2: From [20]: Multi-layer PCB stack-up with ten metal layers. The power and the SPI control have dedicated layers. The stripline layer holds the Wilkinson power dividers. Blind vias carry the connection between the different layers.

metal layers and dedicated power and control signal layers distributed on six layers. Figure 6.2 and Figure 6.3 describe these two stack-ups.

6.3.2 Thermal expansion

This system is for satellites flying in LEO. Since then, the system must withstand a large thermal range. Thermal expansion and contraction will affect the structure. The displacement coming from the temperature variation applies mechanical tensions on the structure, especially near the via-interconnect lines [22]. It also modifies the electrical characteristics of the system [23]. The drawback of using blind vias lies in this mechanical tension that the designer must characterize to ensure the functionality and durability of the circuit.

6.3.3 Power balance and phase difference

To avoid a power unbalance at the different beamformers, we must feed each of them with the same signal power. For that, we must use the same number of power dividers (four) for the 16 chips. Due to the difference in line length, an extra phase shift will appear at the different beamformers. We need to include that in the scanning phase shift.

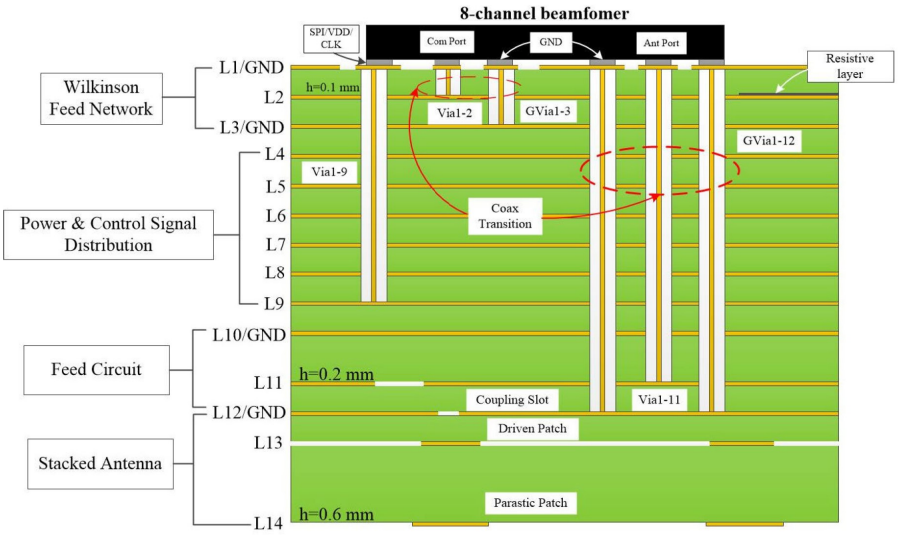

Figure 6.3: From [21]: Multi-layer PCB stack-up with 14 metal layers. They weld the beamformers on top of the stack-up. Blind vias feed the integrated circuits with their different inputs. The Wilkinson feed network divides the RF input and feeds the different beamformers. The power and control signals have dedicated layers. Strip lines excite the antennas through a coupling slot. The parasitic patches optimize the array performance.

6.3.4 Digital control

Other parts of the system need to compute the desired scan angle at an instant. This information must translate into a coefficient set for the 64 elements. Reference [24] proposes a low-cost commercially available ARM-based microcontroller to compute those and feed them to the beamformers. The beamformers IC generally have a small memory capable of holding several coefficients. Nevertheless, these memories are too limited for a complete scan application with a one-degree precision. We require an external memory with all the coefficients stored in a look-up table for fast access. We may send several coefficients at once to the chips depending on the satellite's trajectory. We place those microcontrollers offboard.

6.4 Layout proposal

Taking the previously mentioned elements into account, we can make a first layout proposal. The system is a multi-layer PCB stack-up as the system needs several signals to drive the beamformers properly. The thermal expansion concern motivates using a specific microstrip-to-stripline transition to connect the beamformer to the antennas. The connection is then made through coupling. It also has the advantage of relaxing the manufacturing process as blind vias require several additional process steps depending on the technology. Reference [20] gives an example of possible process steps.

Figure 6.4 gives a representation of the multi-layer PCB stack-up proposal. It has five metal layers with a 0.508 mm thick dielectric layer between two metal layers. Between the first and second metal layers, the thickness of the dielectric is 1.524 mm. The first layer is for the antennas, the third is the antenna's feeding stripline, and the fifth, the layer holding the electronic integrated circuits and the microstrips. Layer four is the ground plane with etched apertures for the microstrip-to-stripline transition, and layer two is a metal plate with etched apertures to couple the striplines with the antennas.

Finally, Figure 6.5 represents a top view of the layout with the placement of the components. The different elements apart from the lines are scaled. The different colors reference the different layers (cf. Figure 6.4). The RF input port is centred to allow the placement of the different power dividers such that each beamformer experience the same additional loss. Each beamformer feeds four antennas and is placed in the middle of a group of four antennas. The distance between antennas is half-wavelength. We notice a total of 64 antennas, 16 beamformers, and 15 power dividers.

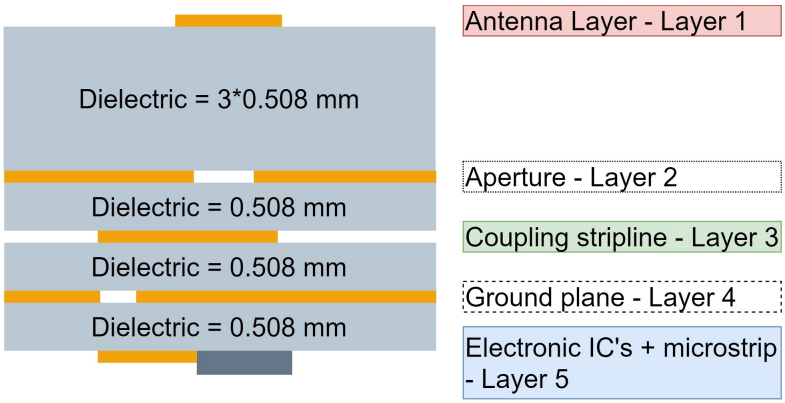

Figure 6.4: Multi-layer PCB stack-up proposal with five layers. We may avoid the blind vias using a specific microstrip to stripline transition.

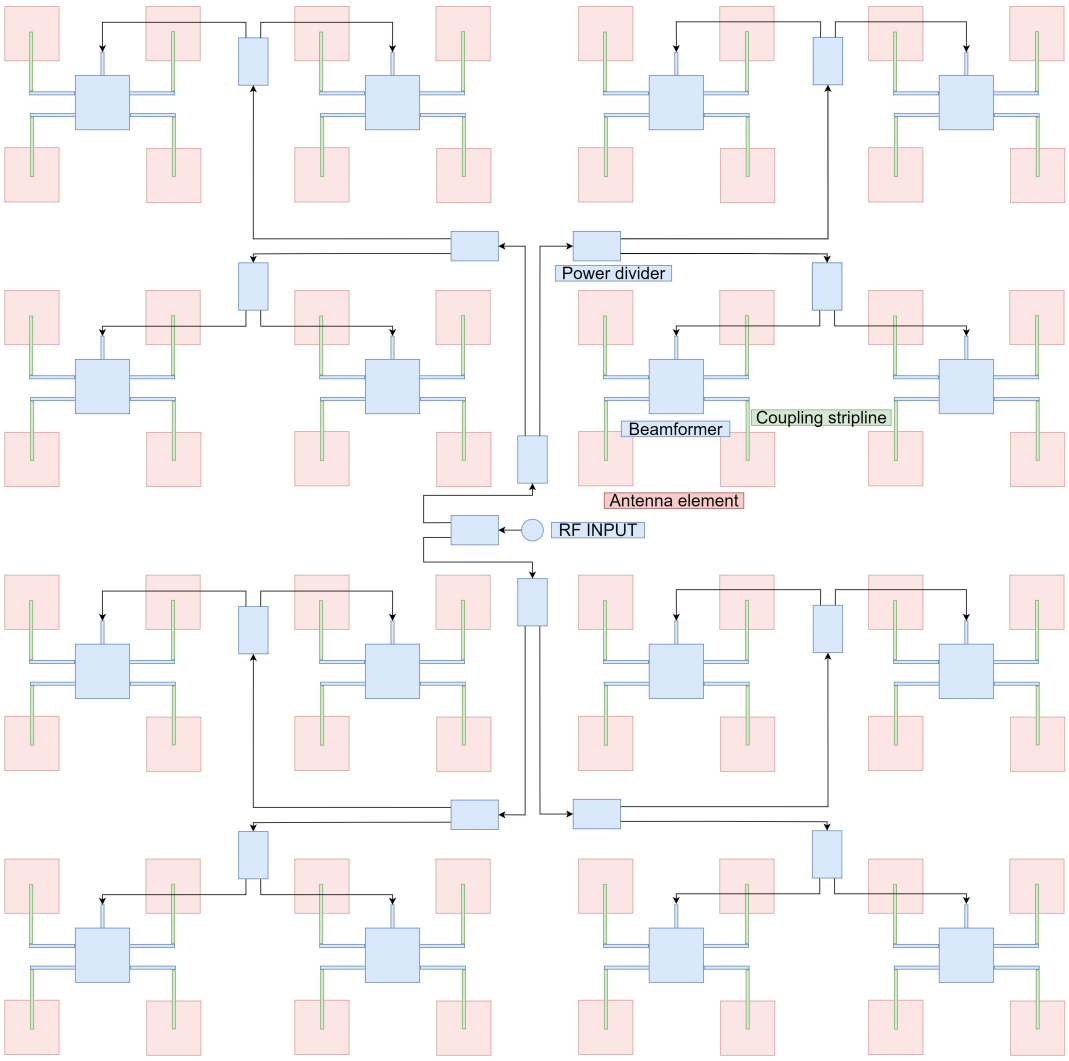

Figure 6.5: Multi-layer stack-up layout proposal.

7 | Antenna design

This last chapter focuses on an antenna design suitable for our application. As introduced in the previous chapter, we plan on having a specific microstrip-to-stripline transition to avoid blind vias in our layout.

Section 7.1 presents a literature review for both aperture-coupled antennas with CP and microstrip-to-stripline transitions. Finally, Section 7.2 gives a comprehensive summary of the antenna design. It also includes a two-by-two antenna array architecture using sequential rotation to improve the axial ratio of the system. CST commercial software has been used throughout the antenna and array design.

7.1 Literature review

7.1.1 Aperture coupled antenna

We consider an aperture coupled patch antenna as it enhances the antenna's impedance bandwidth [25]. The system targets CP with an axial ratio lower than 3 dB.

Reference [26] presents an aperture-coupled annular-ring microstrip antenna for CP. Such an annular-ring shape, offering a smaller patch size than a circular microstrip antenna, uses a single series feed configuration, which excites the required two orthogonal resonant modes. Experimental results prove an achievable CP bandwidth of 8.9% with a center frequency of around 2.5 GHz. We define the CP bandwidth as the bandwidth over which the antenna has an axial ratio lower than 3 dB in the direction of the main beam. The achieved impedance bandwidth is larger than 8.9%. Figure 7.1 gives the antenna geometry.

Reference [27] introduces an aperture-coupled microstrip antenna with switchable polarization. This antenna uses a single series microstrip-line-feed configuration. The ring-slot-coupled microstrip antenna allows producing circular and linear polarizations within the impedance bandwidth, depending on the series stub's length. Experimental results prove an achievable CP bandwidth of 4.4% with a center frequency around 2.525 GHz.

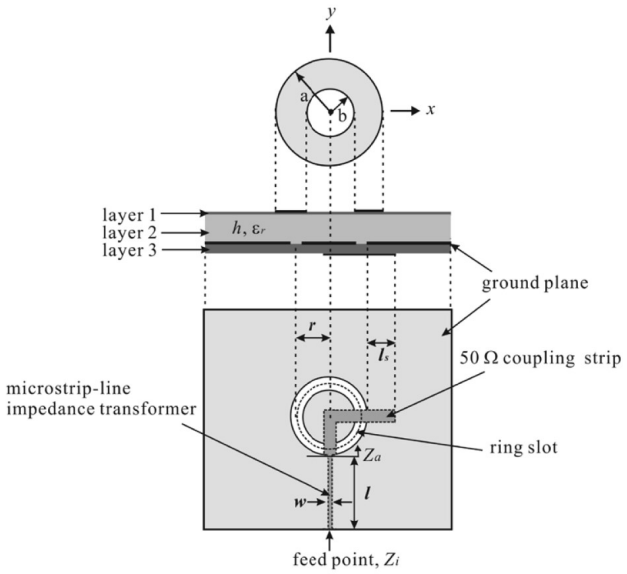

Figure 7.1: From [26]: Aperture-coupled annular-ring microstrip antenna for CP.

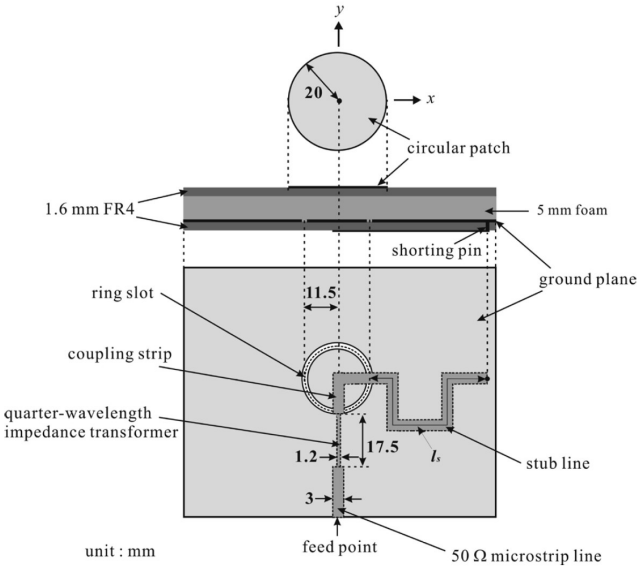

Figure 7.2: From [27]: Aperture-coupled microstrip antenna with switchable polarization using single series microstrip-line-feed configuration.

Reference [28] investigates an aperture-coupled microstrip line feed circularly polarized patch antenna. It uses two different line feeds, one circular arc-line feed and one square arc-line feed visible in Figures 7.3a and 7.3b. The antenna utilizes

four Γ-shaped slots. The geometry offers a CP bandwidth of 78% at broadside and 72% at endfire. The impedance bandwidth is 15% from 3.1 to 3.6 GHz for the circular arc-line feed and 14% from 3.1 to 3.5 GHz for the square arc-line feed.

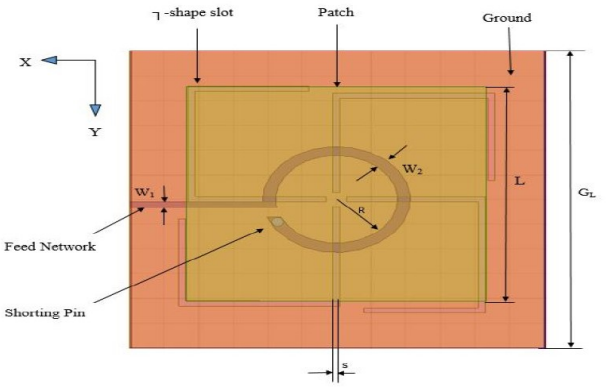

(a) Aperture-coupled microstrip line feed circularly polarized patch antenna utilizing a circular arc-line feed and four Γ-shaped slots.

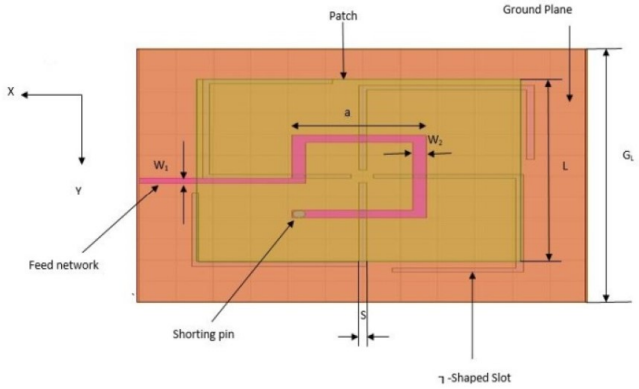

(b) Aperture-coupled microstrip line feed circularly polarized patch antenna utilizing a square arc-line feed and four Γ-shaped slots.

Figure 7.3: From [28]: Aperture-coupled microstrip line feed circularly polarized patch antenna.

Reference [29] showcases a high gain and circularly polarized resonance cavity antenna for X-band. It utilizes an aperture coupled microstrip antenna and a frequency selective surface, an array of circular patches, as a superstrate. The cavity improves the antenna gain while keeping the system compact. It offers a CP bandwidth of 2.4% (200 MHz) centered on 8.2 GHz and a gain of 20.5 dBic (dB isotropic for CP antenna). For beamforming, having directive elements is not optimal.

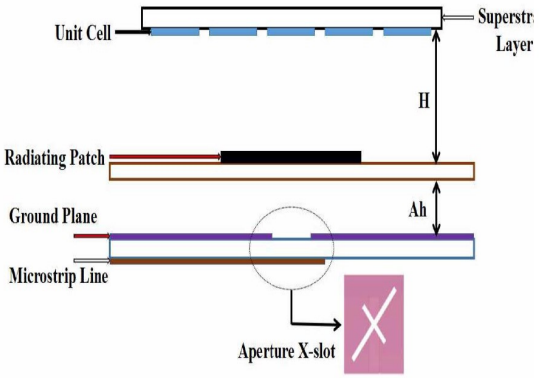

Figure 7.4: From [29]: High gain and circularly polarized resonance cavity antenna for X-band composed of an aperture coupled microstrip antenna and a frequency selective surface, an array of circular patches, as a superstrate.

Finally, Reference [30] presents an aperture-coupled microstrip patch antenna with a crossed slot. It gives a CP bandwidth of approximately 20%. This geometry is the base for the antenna design of this document. That is because it offers good performance while having a low manufacturing complexity.

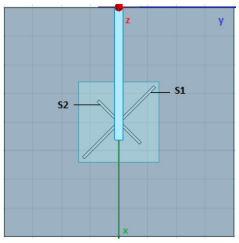

(a) Model: Top view

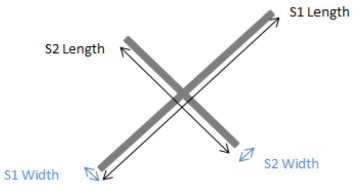

(b) Slots

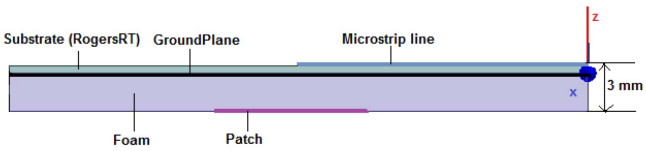

(c) Model: Side View

Figure 7.5: From [30]: Aperture-coupled microstrip patch antenna with crossed slot.

7.1.2 Microstrip-to-stripline transition

Thermal expansion motivates the investigation of a specific microstrip-to-stripline transition (cf. Section 6.3). Similar to the aperture-coupled antennas, we want to couple the stripline and the microstrip through an aperture. This transition is rare in the scientific literature. We focus this state-of-art review on Microstrip-to-Slotline (MS-SL) and Microstrip-to-Microstrip (MS-MS) transitions.

Let us start by presenting a MS-SL transition. The authors build a double transition to have two ports: one feeding port and one measuring port to measure such structure. Reference [31] showcases a simple 90° crossing transition between the microstrip and the slot-line. Using radial stubs allows for a broader bandwidth than straight ones. The microstrip open circuit radial stub should appear as a short circuit and the slot-line short circuit radial stub as an open circuit at the crossing reference plane. From there comes the extensions of approximately 90 degrees on slot and microstrip sides. Figure 7.6 depicts the transition geometry. It has two transitions in cascade for measurement purposes. Finally, Figure 7.7 gives the measured and simulated S_{21} parameter. It shows good agreement between simulation and practice. The passband goes from 3 to 15 GHz, and the insertion loss is below 1.3 dB on the band ranging from 3.2 to 15.5 GHz. As the transition is double, a simple transition would only introduce half the insertion loss, which is 0.65 dB.

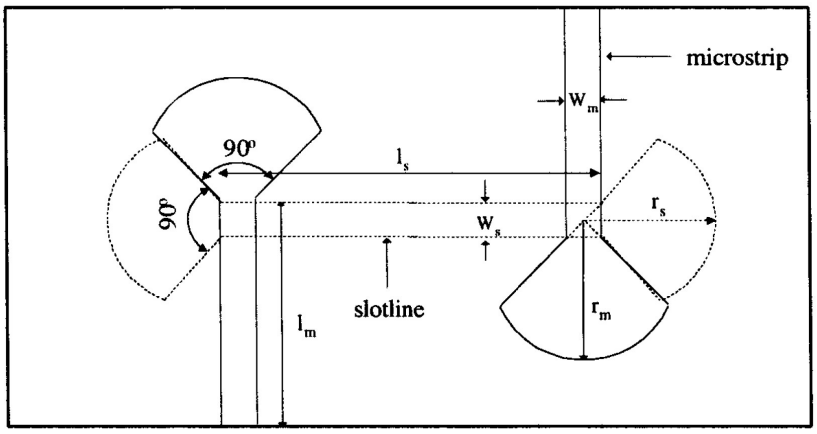

Figure 7.6: From [31]: MS-SL transition. Geometry of two transitions in cascade and their dimensions. The transition is a 90° crossing using radial stubs for both the microstrip and slot-line.

We now focus on the Microstrip-to-Microstrip (MS-MS) transitions. Reference [32] presents a wideband vertical MS-MS transition. The wide bandwidth comes from the use of two similar microstrip lines aligned on top of each other and

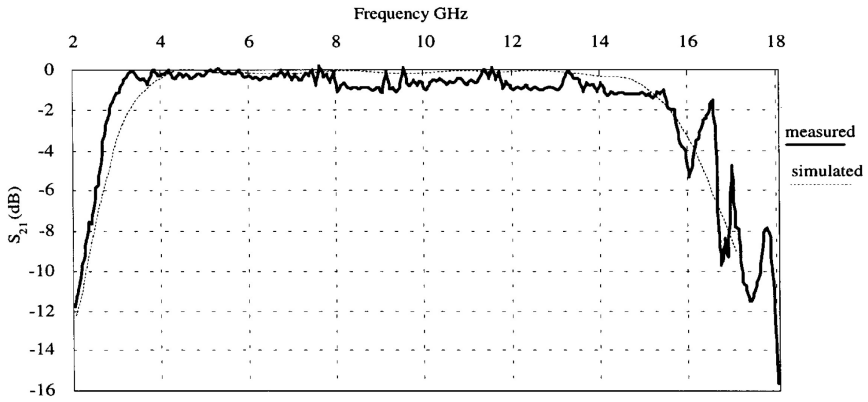

Figure 7.7: From [31]: Transmission coefficient of the double transition cascading depicted in figure 7.6.

perpendicularly coupled with a uniform slot-line resonator on the ground plane. They achieve three-pole filtering by setting the slot-line length θ_s to 90° at the operating frequency and extending the microstrip's electrical length θ_m to 90°. Figure 7.8 gives top and side views of the transition's geometry, and 7.9 compares the measured and simulated transmission coefficients S_{21} and S_{11}. The 1-dB bandwidth ranges from 3.61 to 8.16 GHz.

Reference [33] introduces a broadband MS-MS vertical transition based on broadside coupling between the upper and lower microstrip patches through a wide slot etched on the ground plane. The authors add an extra patch on the ground plane to further enhance the bandwidth, introducing a half-wavelength resonance into the passband. The patch lengths are a quarter-wavelength. The width of the extra patch is narrower than the slot's width. Figures 7.10 and 7.11 depict the geometry of the two transition versions. Finally, Figure 7.12 gives the transition's transmission coefficients with maximum and minimum insertion losses of 2.1 dB and 0.7 dB in the passband, respectively.

Reference [34] investigates a wideband MS-MS vertical transition using an opencircuited slot-line stepped-impedance resonator. The impedance ratio of the stepped-impedance resonator control allows placing two transmission zeros to improve the passband selectivity, offering about out-of-band suppression of about 22 dB. The transition is between two open-circuited microstrip lines connected to feeding lines perpendicularly coupled through a slot-line stepped-impedance resonator. Figure 7.13 gives the geometry of the transition, and 7.14, the transmission coefficients.

Finally, Reference [35] presents a MS-MS vertical transition with slot-line stepped-impedance resonator, which offers a wideband filtering response with an extended upper stopband. It has two open-circuited microstrip lines printed on the

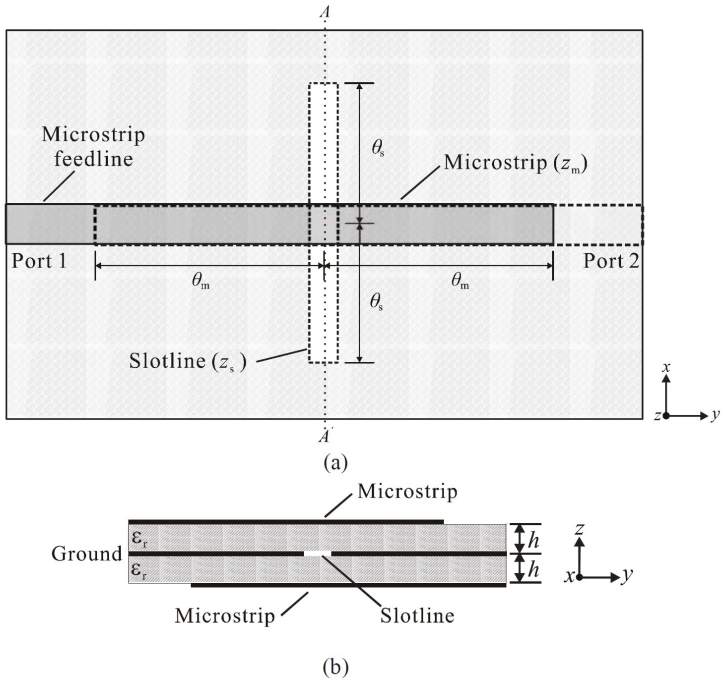

Figure 7.8: From [32]: Wideband vertical MS-MS transition. It has two identical microstrip lines aligned on top of each other and perpendicularly coupled with a uniform slotline resonator on the ground plane.

top and bottom layers and a stepped-impedance slot-line resonator etched on the common ground plane. Figure 7.15 gives the transition geometry, while Figure 7.16 describes its transmission coefficients. It has a 2-dB insertion loss ranging from 1.64 to 4.02 GHz and a stopband attenuation of more than 12.1 dB between 4.78 and 16.75 GHz.

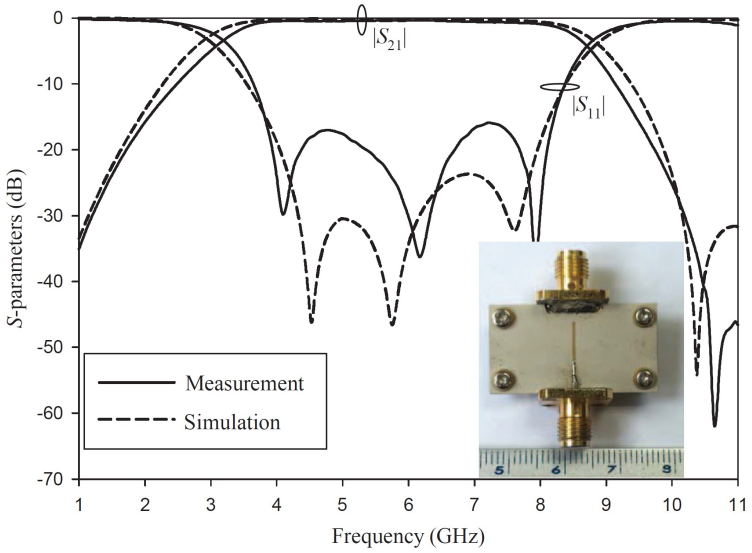

Figure 7.9: From [32]: Transmission coefficient of the wideband vertical MS-MS transition.

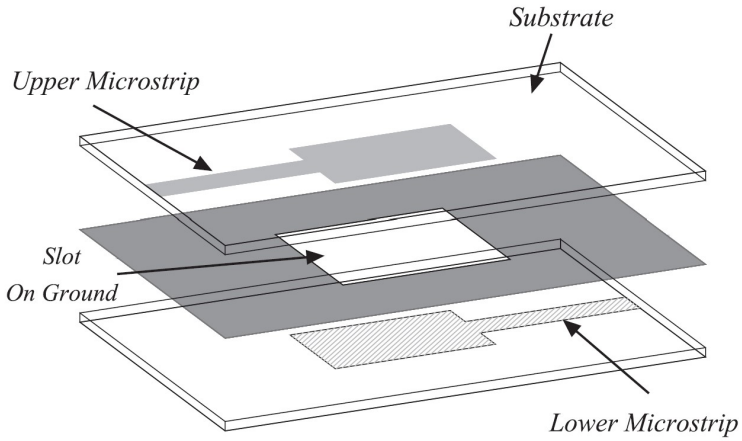

Figure 7.10: From [33]: Broadband MS-MS vertical transition based on broadside coupling between the upper and lower microstrip patches through a wide slot etched on the ground plane.

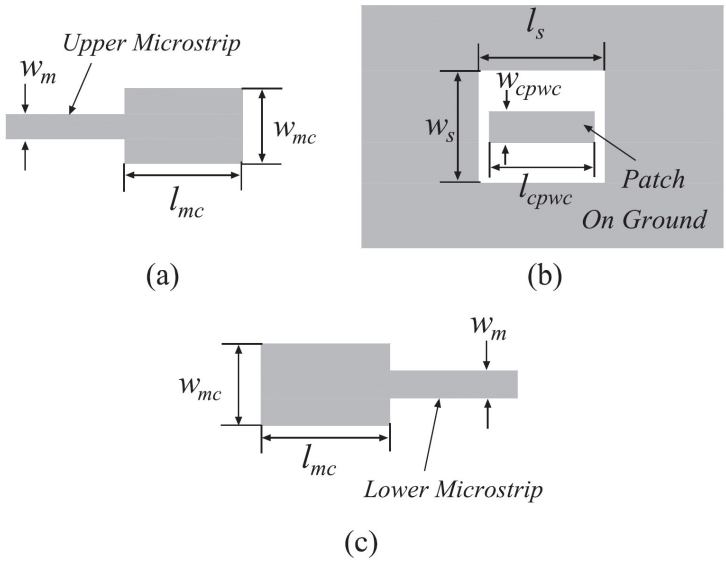

Figure 7.11: From [33]: An extra patch on the ground plane introduces a half-wavelength resonance into the passband.

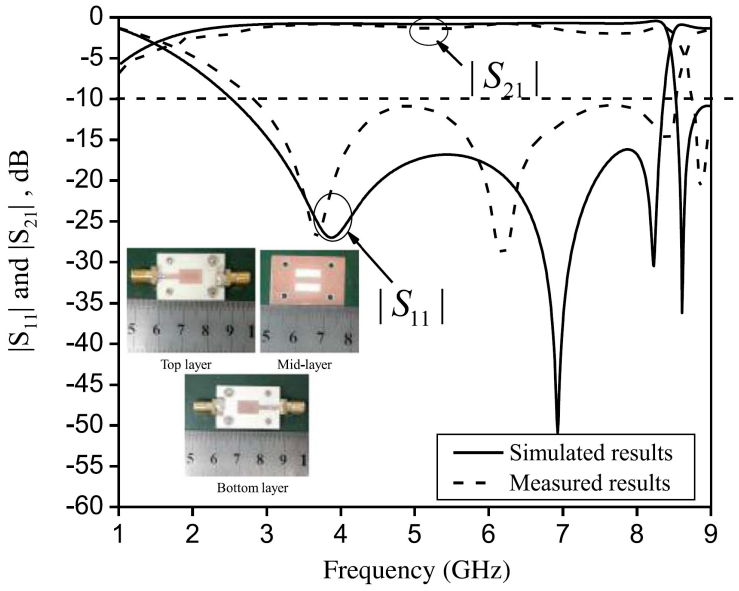

Figure 7.12: From [33]: Transmission coefficients of the vertical MS-MS transition.

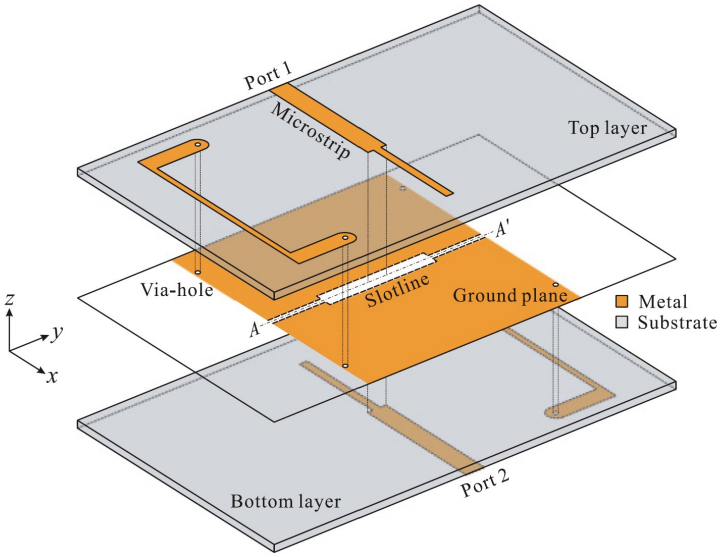

Figure 7.13: From [34]: Wideband MS-MS vertical transition using open-circuited slot-line stepped-impedance resonator.

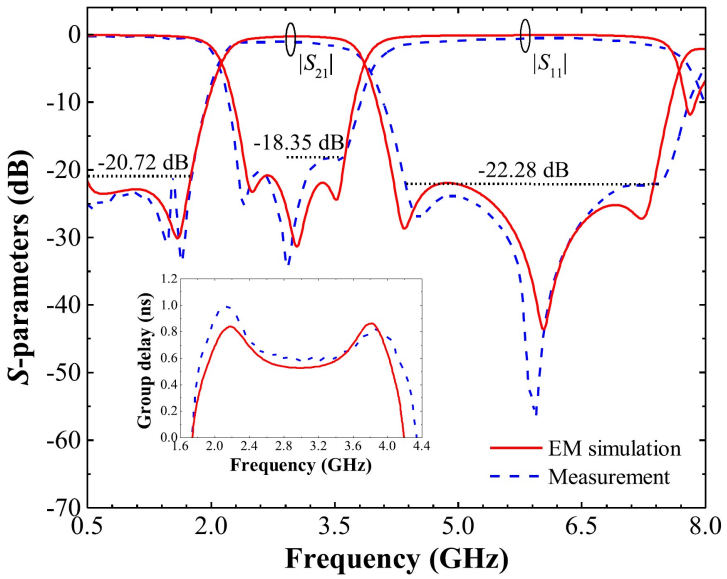

Figure 7.14: From [34]: Transmission coefficients of the vertical MS-MS transition.

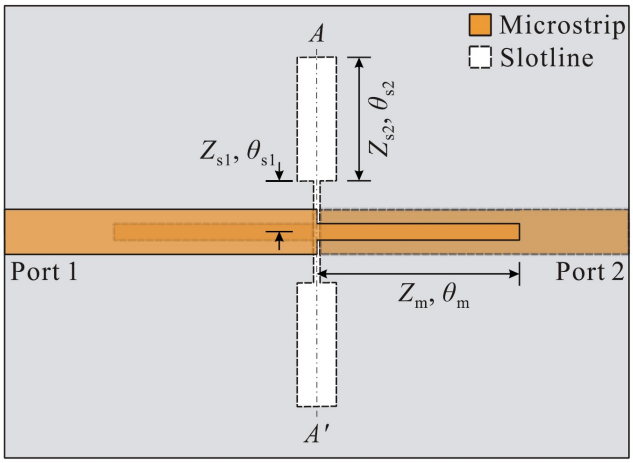

Figure 7.15: From [35]: MS-MS vertical transition with slot-line stepped-impedance resonator.

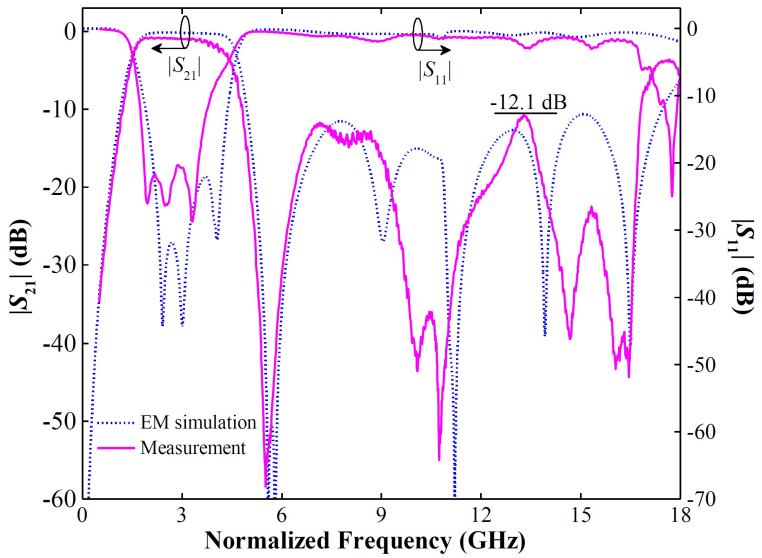

Figure 7.16: From [35]: Transmission coefficients of the vertical MS-MS transition.

7.2 Design of array and feeding lines

This section presents the design of an antenna element similar to the geometry proposed in Reference [30], an aperture-coupled microstrip square patch antenna. We add a specific microstrip-to-stripline transition to avoid using blind vias.

7.2.1 Single element design

The antenna is a five-metal layer stack-up, as depicted in Figure 6.4. The second layer holds the crossed slot aperture (centered to the square patch) used to couple the stripline of the third layer with the antenna square patch. The fourth layer is the ground plane. Rectangular slots tilted by 45°, responsible for the coupling between the microstrip line and the stripline, are etched on this fourth layer. That allows avoiding blind vias for the transition between the beamformers and the antennas. Notice that we place a layer of dielectric (Rogers RO4003C) having a thickness of 0.508 mm between two metal layers. The layer between the antenna and its aperture has a thickness of 1.524 mm. Figure 7.17 gives a geometrical representation of the antenna element, and Table 7.1, its corresponding dimensions. Note that the colors correspond to the layers depicted in Figure 6.4. For the antenna simulation, we center the square patch on a 3.6 by 3.6 cm square stack-up. We connect the microstrip line to a waveguide port and connect the metal layer underneath the microstrip (layer 4) to the ground.

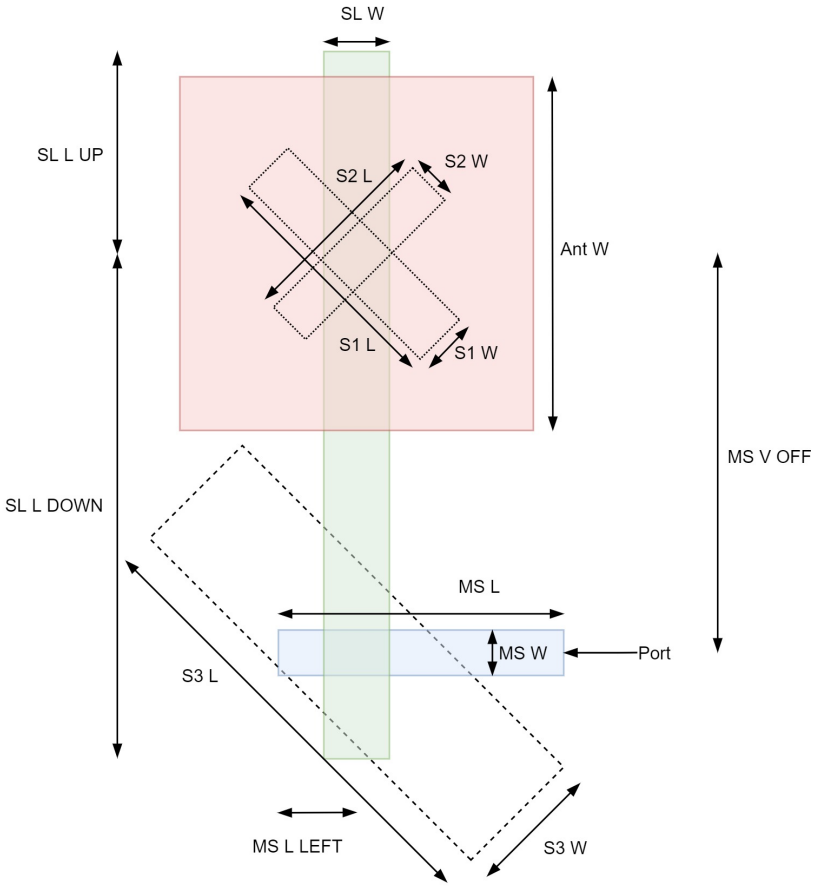

Figure 7.17: Geometry of the antenna.

Parameter	Value [mm]	Parameter	Value [mm]
Ant W	7.6	S2 W	0.9
SL W	1.3	S3 W	2.602
SL L UP	3.758	S3 L	8.991
SL L DOWN	9.891	MS W	0.75
S1 L	4.8	MS L	7.3748
S1 W	1.102	MS V OFF	7.35
S2 L	3.9	MS L LEFT	1.7248

Table 7.1: Antenna geometry dimensions.

7.2.2 Antenna performance

We present in this section different figures of merit of the antenna. First, Figure 7.18 presents the antenna directivity and the upper bounded axial ratio at 8.4 GHz. Then, Figure 7.19 showcases the real and imaginary parts of the electric field above the two apertures and the square patch. The application requires an impedance

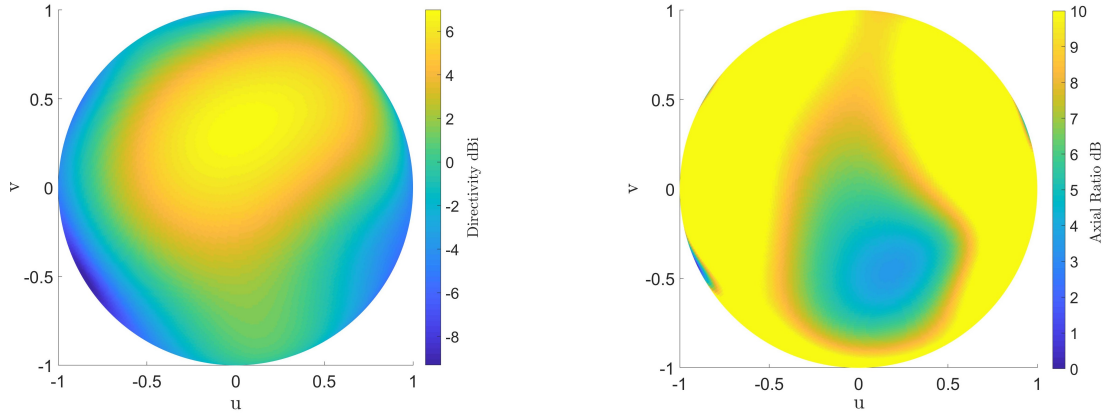

(a) Directivity.

(b) Axial ratio upper bounded at 10 dB.

Figure 7.18: Far-field radiation pattern characteristics of the single antenna at 8.4 GHz.

bandwidth ranging from 8.025 to 8.4 GHz. The system targets a CP with an axial ratio lower than 3 dB. Figures 7.20 and 7.21 give the element co-polar directivity and axial ratio, respectively. We notice that the co-polar directivity suffers from the substantial axial ratio for the frequencies close to 8.025 GHz. Indeed, the antenna's polarization is linear, close to 8.025 GHz, and eventually becomes more circular as the frequency goes towards 8.4 GHz. We notice an axial ratio of 6 dB at 8.4 GHz and an optimum co-polar directivity close to 8.35 GHz.

Figure 7.22 gives the S_{11} parameter of the antenna. We notice a 10-dB range going from 7.947 to 8.471 GHz, which corresponds to a 6.4% bandwidth. Finally, Figure 7.23 gives the total efficiency of the antenna. We define total efficiency as the ratio between the radiated power and the input power. The antenna (including feeding lines) has an efficiency ranging between 73 and 87 % on the band of interest.

During the design of the antenna, the most important design criterion was the impedance bandwidth. Unfortunately, the polarization is not currently optimized. We thus do not have CP but a linear polarization. Still, we achieved an impedance bandwidth matching the application requirements.

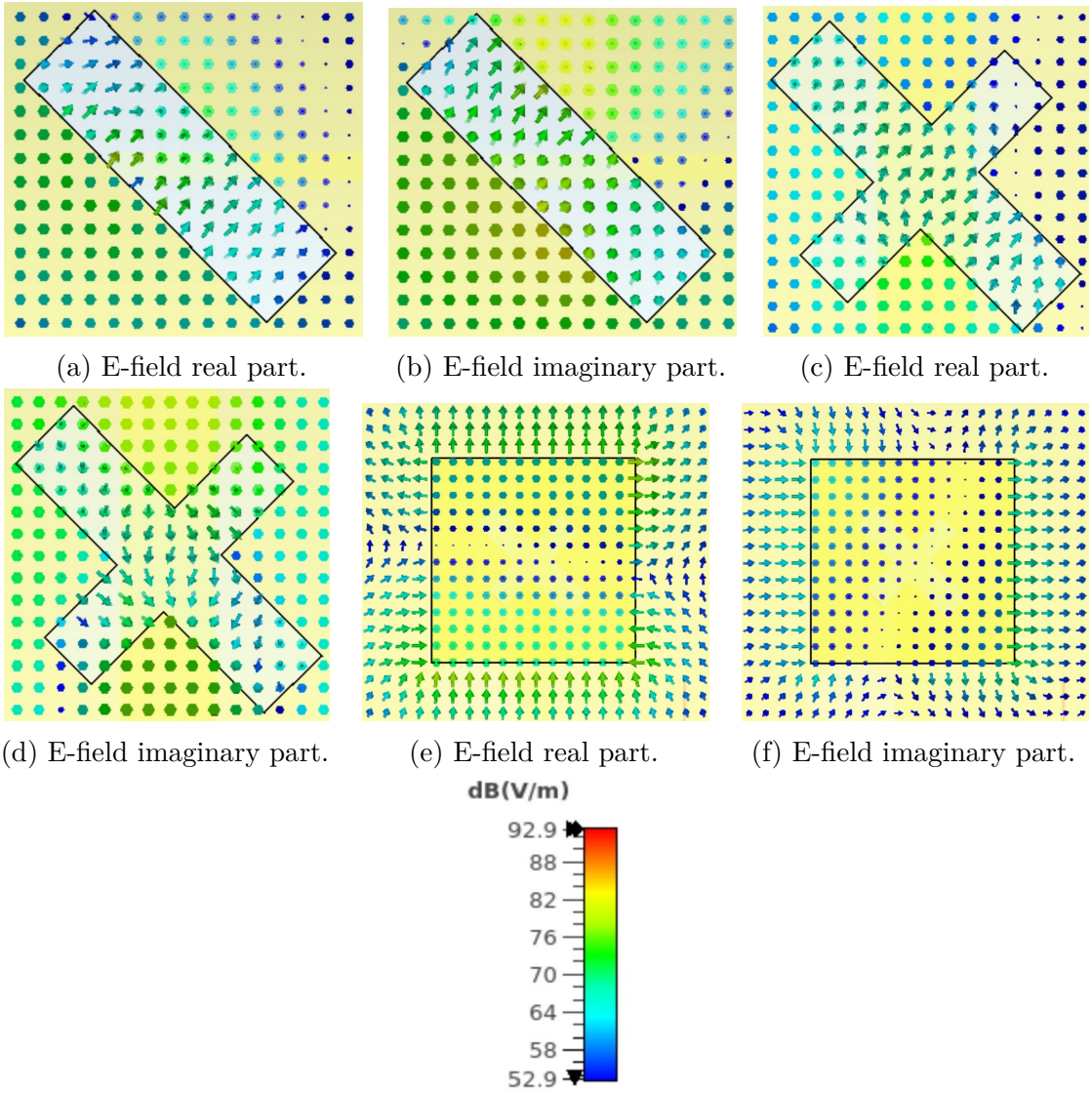

(a) E-field real part. (b) E-field imaginary part. (c) E-field real part.

(d) E-field imaginary part. (e) E-field real part. (f) E-field imaginary part.

Figure 7.19: E-field above the two apertures and the square patch at 8.4 GHz.

7.2.3 Antenna array architecture

We are now interested in building a two-by-two elements array with the antenna described in Section 7.2.1. To improve the axial ratio of the system without modifying the antenna design, we sequentially rotate the elements by 90° and feed them with signals sequential phase shifted by 90° [36]. Figure 7.24 gives a representation of the array. The spacing between the elements is half-wavelength.

Building this setup on CST allows us to benchmark it. We care about the S-parameters, the active S-parameters for the zenith scan, and the total antenna

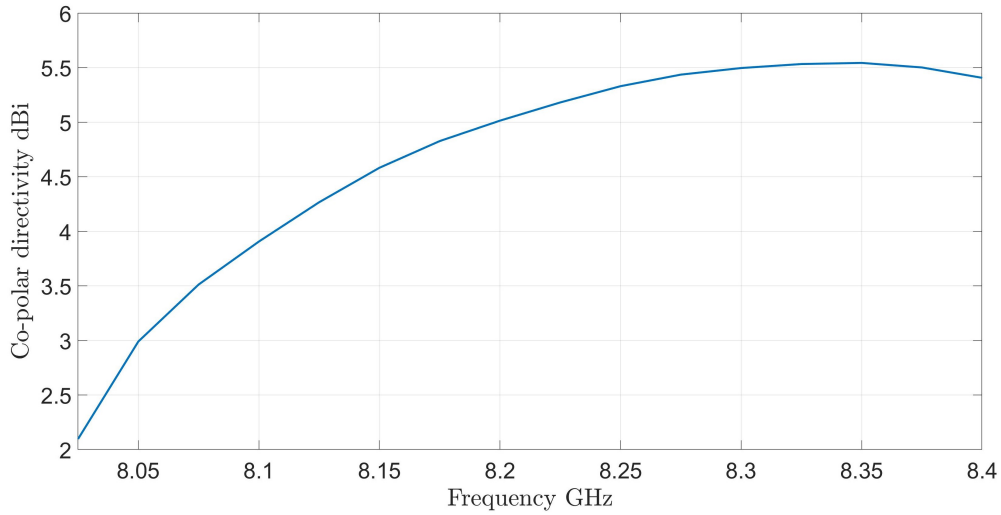

Figure 7.20: Single antenna co-polar directivity vs. frequency for $\theta = \phi = 0°$.

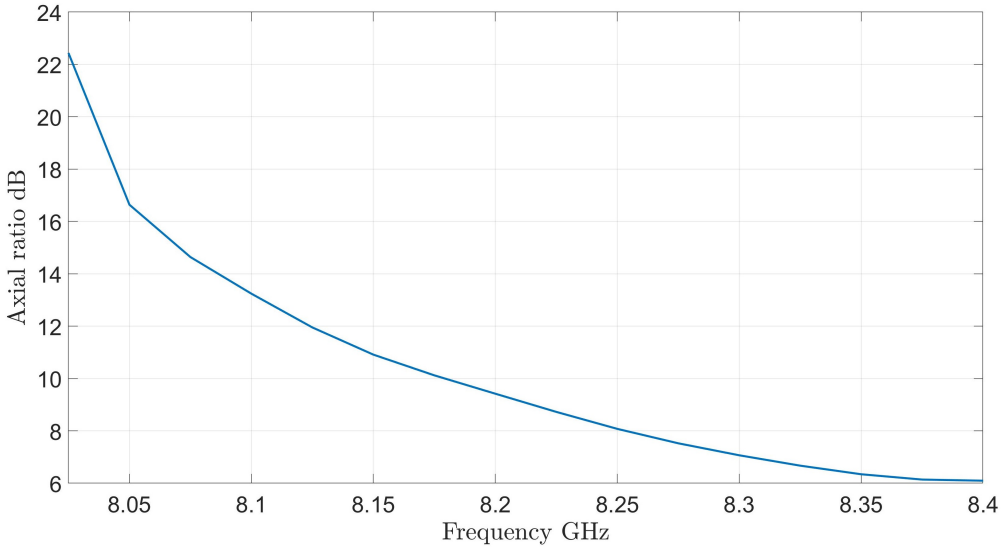

Figure 7.21: Single antenna axial ratio vs. frequency for $\theta = \phi = 0°$.

efficiency in the presence of the other antennas. We then introduce the proper phase shifts to scan in four directions.

Figures 7.25 and 7.26 give the first port's S-parameters and active S-parameters, respectively. The other ports' S-parameters are similar as the system is symmetric. We notice a slight shift for the S_{11} parameter compared to the single element's one. That gives an impedance bandwidth of 6.51% and active impedance bandwidth of 4.77% (from 8.067 to 8.544 GHz). Figure 7.27 depicts the total efficiency for the

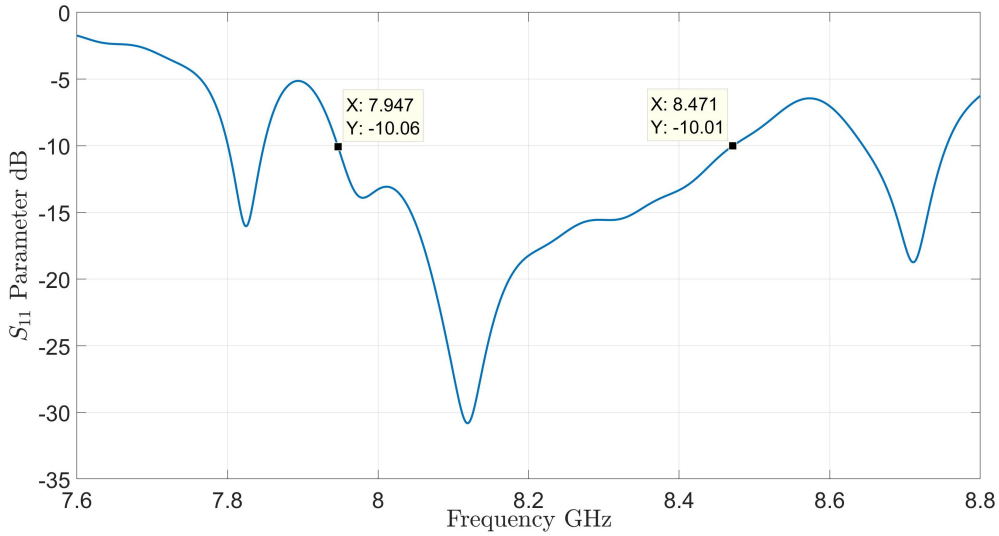

Figure 7.22: Single antenna S_{11} parameter vs. frequency.

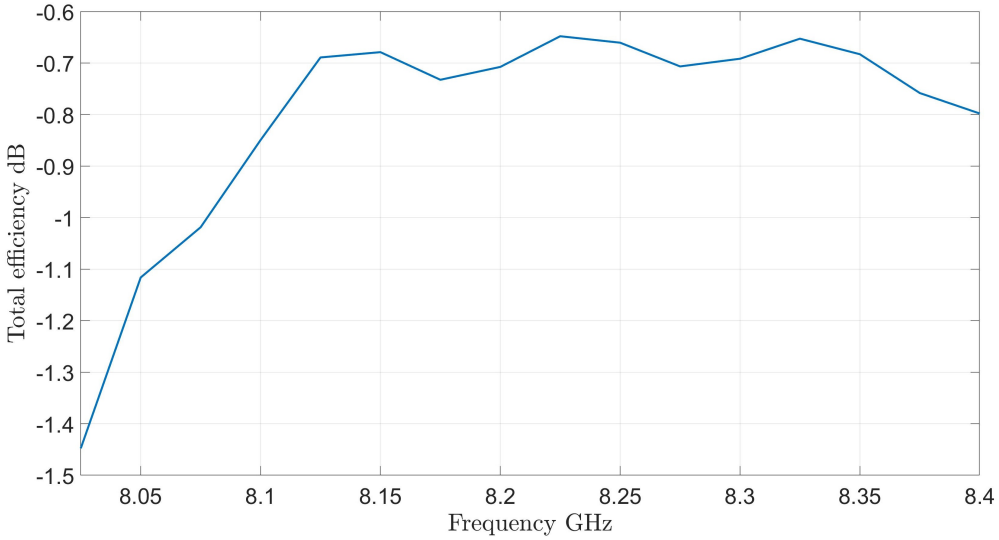

Figure 7.23: Single antenna total efficiency vs. frequency.

four different ports of the array. Those are similar and correspond to an efficiency ranging from 63.1% to 79.4%. We notice that placing the antenna in an array degrades its efficiency and impedance bandwidth.

We now compute the proper weights to scan a beam in four different positions. We use unit amplitudes and phase shifts as in Table 7.2. Figures 7.28, 7.29, and 7.30 depict cuts in the $\phi = 0°$ plane of the array co-polar directivity at three different frequencies and four different sets of weights. We notice that the sequential rotation

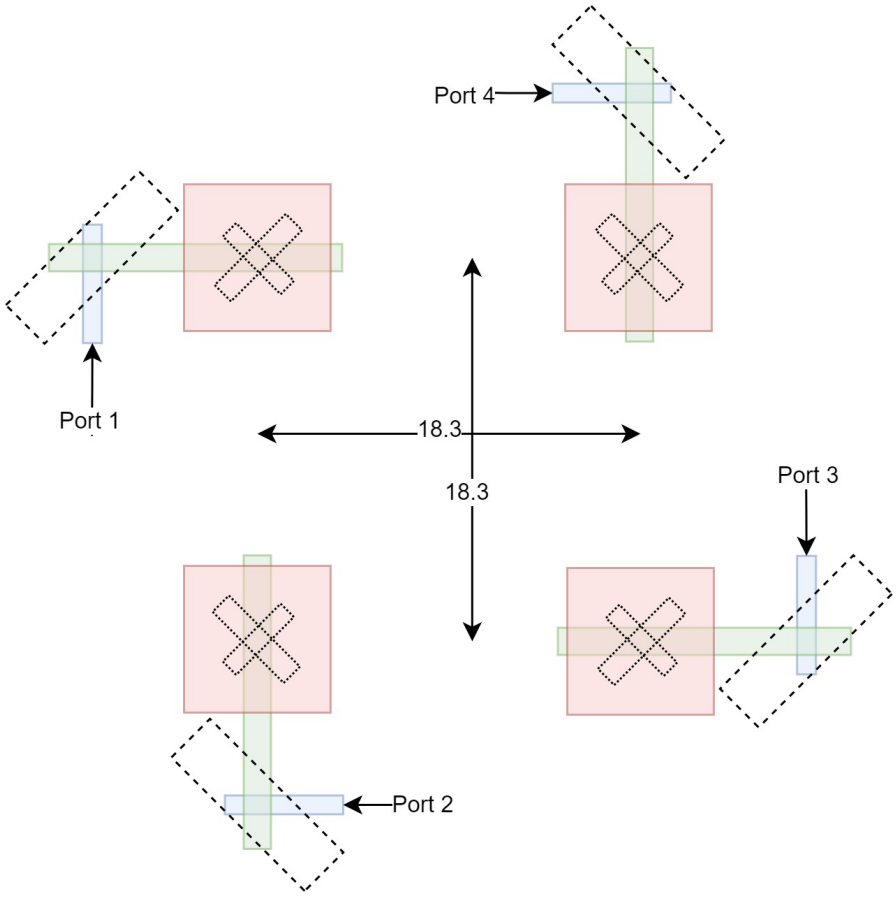

Figure 7.24: Two-by-two elements array representation. We space patches by a half-wavelength.

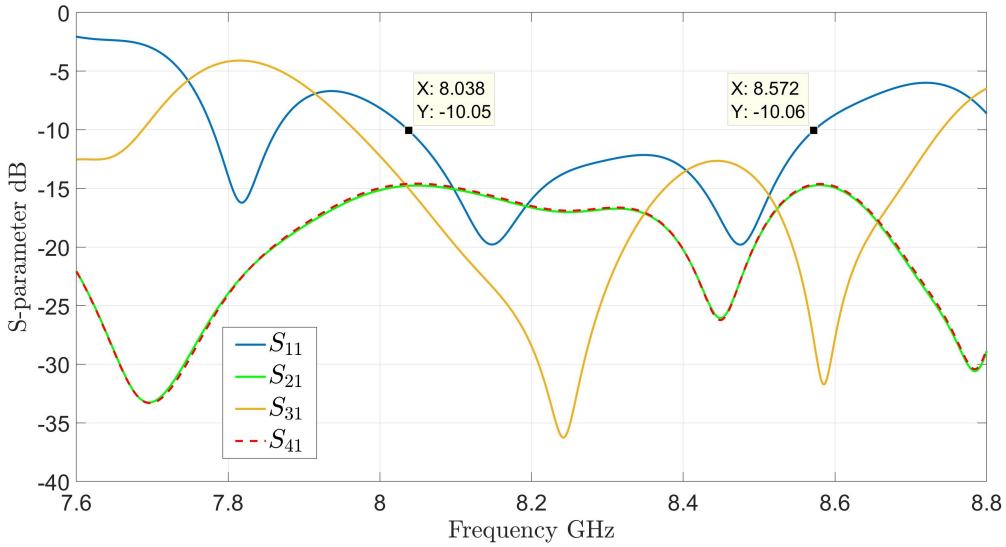

Figure 7.25: Array first port S-parameters vs. frequency.

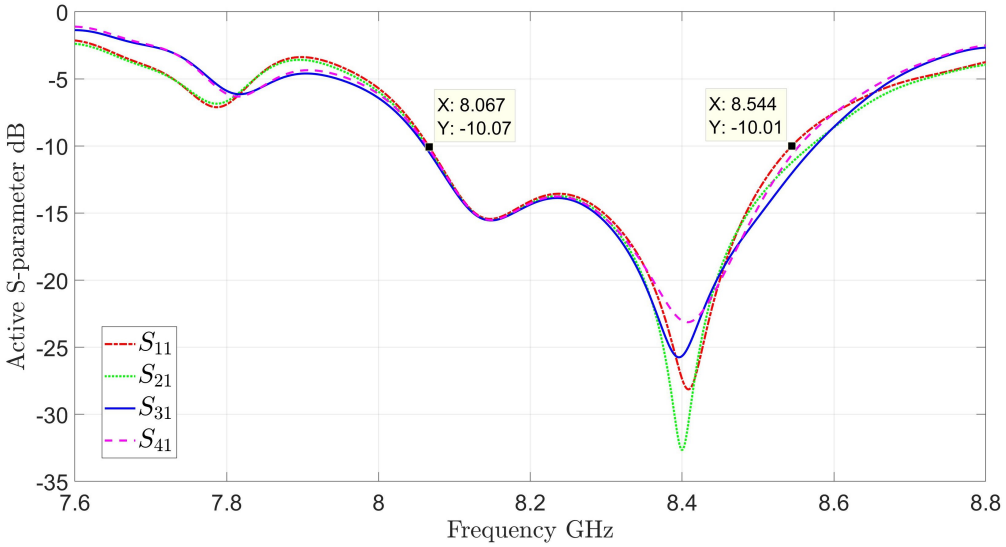

Figure 7.26: Array first port active S-parameters for the default weights (sequentially increasing phase shifts).

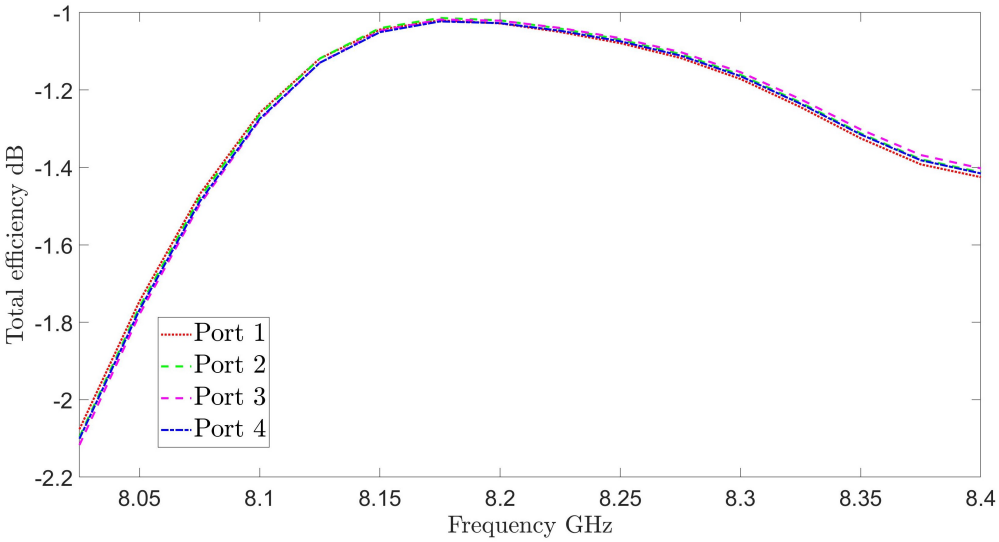

Figure 7.27: Array ports total efficiencies vs. frequency.

Scan (θ,ϕ)	Port 1 phase	Port 2 phase	Port 3 phase	Port 4 phase
(0°,0°)	0°	90°	180°	270°
(30°,0°)	0°	90°	90°	180°
(45°,0°)	0°	90°	52.72°	142.72°
(60°,0°)	0°	90°	24.11°	114.11°

Table 7.2: Phase shift vectors for four different scan angles.

yields an excellent axial ratio at a zero-degree elevation angle, which degrades as the elevation angle increases. Consequently, the system achieves higher co-polar directivity as it suffers less from polarization mismatch. We compare those values to the ones obtained using the MATLAB simulation tool developed in Section 5.3. We observe similar evolution of the directivity with elevation angle. Still, the MATLAB simulation exhibits better performance and remains a first-order approximation.

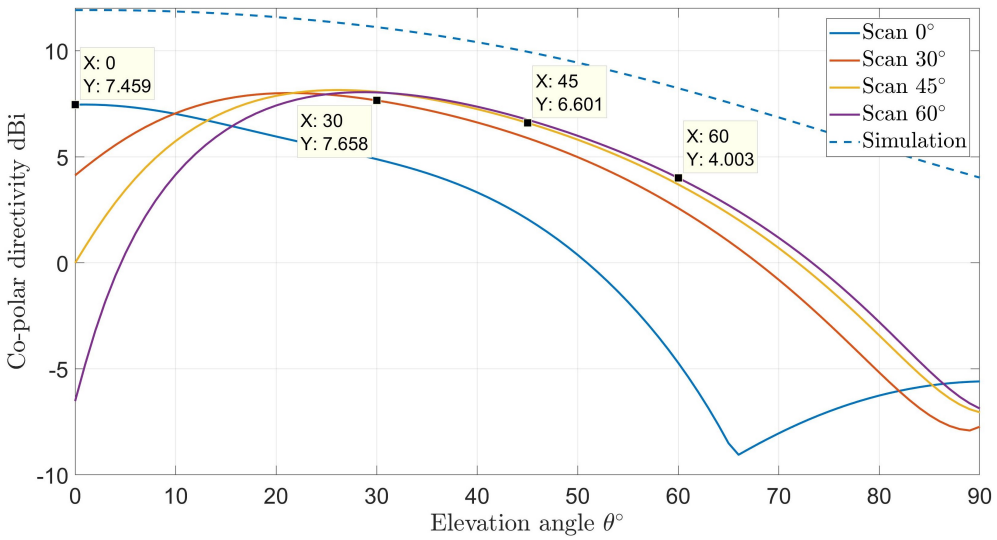

Figure 7.28: Array co-polar directivity vs. elevation angle for different scan weights. Cut in $\phi = 0$ plane, far-field simulation at 8.025 GHz.

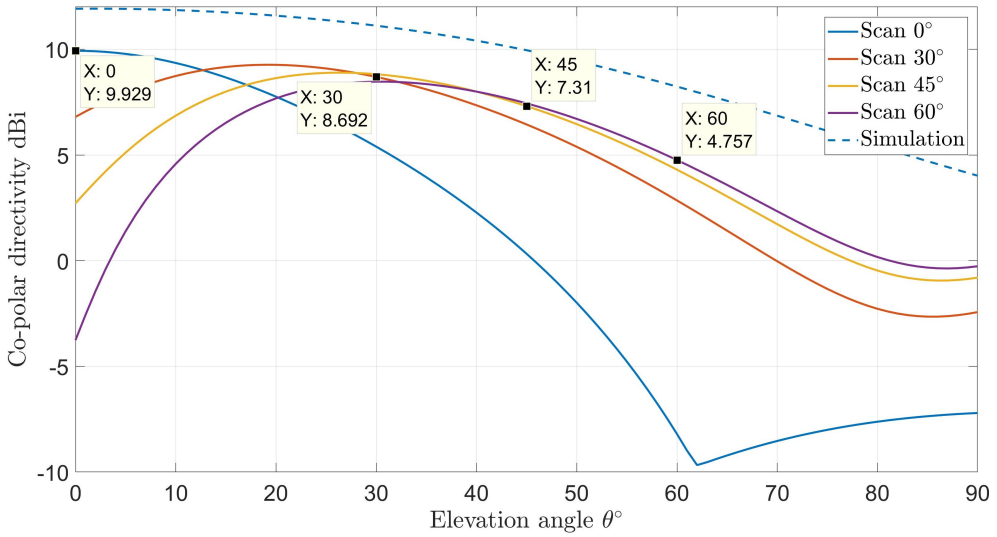

Figure 7.29: Array co-polar directivity vs. elevation angle for different scan weights. Cut in $\phi = 0$ plane, far-field simulation at 8.2 GHz.

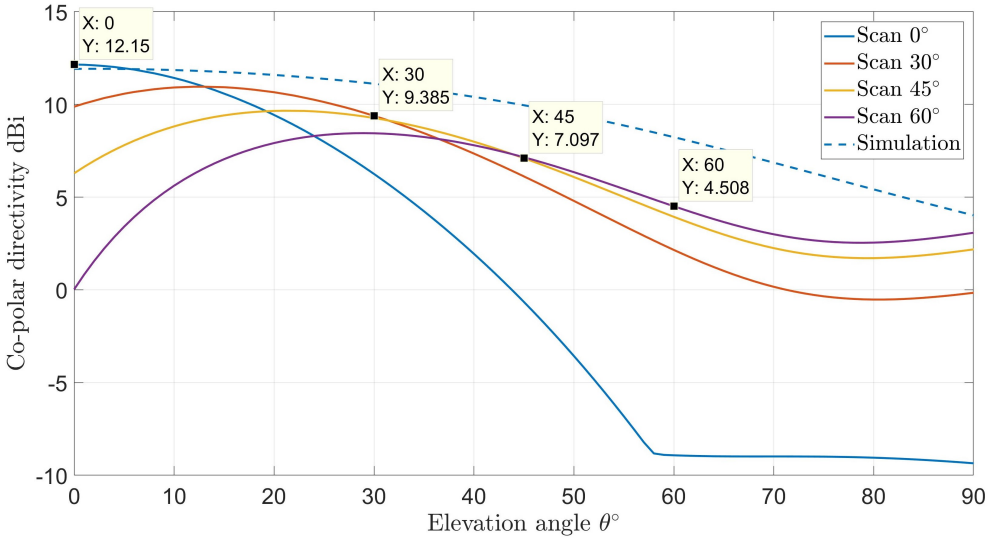

Figure 7.30: Array co-polar directivity vs. elevation angle for different scan weights. Cut in $\phi = 0$ plane, far-field simulation at 8.4 GHz.

8 | Conclusions and future work

The goal of the master thesis was to design an X-band antenna system capable of beamsteering to increase the link data throughput between the satellite and the ground station. Indeed, the high transmitter gain allows to improve the SNR at the receiver and, therefore, permits higher modulation orders leading to improved spectral efficiency. The broad bandwidth of 375 MHz (reserved by the ITU for such applications) and high spectral efficiency allow for high throughput. The extensive scanning range is also of interest because the satellite does not fly strictly above the ground station. Narrowing this range too much would lead to a reduced time over which the system can close the link, and that is a reduced amount of data transmitted in total.

This document addresses this problem, dividing the design procedure into several steps, elaborating a link budget to study the project feasibility and predicting the achievable data rate. We note that the application requires a co-polar gain of 7.7 dB to close the link and that the specified 18 dB gain would allow transmission up to 2.2 bits per symbol sent by satellite in the worst case. The system polarization plays a crucial role as it can decrease the co-polar directivity up to 3 dB compared to the total directivity. Using a linear antenna for the transmitter and considering perfect circular polarization in the receiver would lead to a minimum directivity of 10.7 dBi to close the link.

We investigated whether to conform the antenna array to a tri-dimensional shape to improve the system scanning range. Indeed, for a planar array, the directivity decreases as the cosine of the elevation angle. Conformal arrays allow to have some antennas facing the direction of observation and mitigate the directivity decrease for high elevation angles. We thus comprehensively compared two different conformal phased array antennas and a planar phased array antenna. After comparison, the planar antenna stands out for such application as it allows maximal power transmission and presents better directivity for the targetted scan range. In addition, it will enable reducing the system manufacturing and design complexity.

As we aim at fabricating such a high gain antenna in the future, we must take the layout and electronic circuits aspects into account. Based on several criteria,

we scanned the manufacturer catalogs for suitable beamformers and power dividers references. We selected two components corresponding to the system requirements. We proposed the first layout with the placements of the electronic IC's, feeding lines, power dividers, and antennas. Due to the system complexity and the choice of aperture coupled antennas to improve the bandwidth, a multi-layer approach is preferred. Furthermore, as space application deals with high-temperature gradients, we tried to avoid dealing with blind vias as those experience high mechanical stress.

Last but not least, we designed an aperture coupled antenna. Such antennas allow for a high impedance bandwidth desired for this specific application. This aperture coupled antenna also has a specific microstrip-to-stripline transition—the two feeding lines being coupled through a 45° rectangular aperture. As a result, the antenna has a broad impedance bandwidth and total radiation efficiency of up to 87%. The next step was to place the antenna in an array of two-by-two elements sequentially rotated by 90° to improve the axial ratio of the system. The full-wave simulation on CST displays the scanning capabilities of the system.

This document can serve as a base for future developments:

- Building a larger array from the two-by-two array developed in this work is the logical next step to check the achievable co-polar gain over the scanning range. To maintain a sufficiently good axial ratio, we could maintain the nested sequential rotation approach for the four elements sub-arrays and extend it for the full array. Reference [20] presents a 16-elements four-by-four phased array antenna using nested sequential rotation to improve the axial ratio of the system. Such design could be tested with the antenna developed during this thesis to investigate the system performance.

- During the antenna design, the central figure of merit was the impedance bandwidth. Consequently, the antenna polarization is not circular, principally close to 8.025 GHz, where the axial ratio is close to 20 dB. The aperture coupled antenna designed in [30] on which we based our design has a circular polarization. It would be beneficial for the co-polar directivity to improve the axial ratio of the antenna.

- As the goal is to fabricate such a high gain antenna system working at X-band, it is required to investigate the layout aspect more closely. Indeed, the antenna we proposed needs to connect to the different beamformers. Applying the sequential rotation implies additional complexity to drives the different elements.

- Finally, it is interesting to benchmark this microstrip-to-stripline transition without the antenna and study its working principle in more details.

Bibliography

[1] Ag2gaeh, *File:kugelkoord-lokale-basis-s.svg*, Oct. 2015. [Online]. Available: https://commons.wikimedia.org/wiki/File:Kugelkoord-lokale-Basis-s.svg.

[2] C. Christophe, *Lecture notes in antennas and propagation.*

[3] "Properties of antennas," in *Modern Antenna Design*. John Wiley Sons, Ltd, 2005, ISBN: 9780471720614. DOI: https://doi.org/10.1002/0471720615. eprint: https://onlinelibrary.wiley.com/doi/pdf/10.1002/0471720615. [Online]. Available: https://onlinelibrary.wiley.com/doi/abs/10.1002/0471720615.

[4] D. Pozar, *Microwave Engineering, 4th Edition*. Wiley, 2011, ISBN: 9781118213636.

[5] S. Karki and C. Craeye, "Design and modeling of circularly polarized conical beam antennas for space missions.," http://hdl.handle.net/2078.1/210254, Ph.D. dissertation, UCLouvain, Dec. 2018.

[6] *Worldwide elevation finder*. [Online]. Available: https://elevation.maplogs.com/poi/svalbard_satellite_station_svalsat_svalbard_and_jan_mayen.472054.html.

[7] D. Barbarić, J. Vuković, and D. Babic, "Link budget analysis for a proposed cubesat earth observation mission," in *2018 41st International Convention on Information and Communication Technology, Electronics and Microelectronics (MIPRO)*, 2018, pp. 0133–0138. DOI: 10.23919/MIPRO.2018.8400026.

[8] *Digital video broadcasting (dvb); implementation guidelines for the second generation system for broadcasting, interactive services, news gathering and other broadband satellite applications; part 1: Dvb-s2 technical report*, TR 102 376-1 (V1.2.1), European Telecommunications Standards Institute (ETSI), Nov. 2015.

[9] O. Afelumo, A. Awoseyila, and B. Evans, "Simplified evaluation of apsk error performance," *Electronics Letters*, vol. 48, no. 14, pp. 886–888, 2012, ISSN: 0013-5194.

[10] L. Jordanova, L. Laskov, and D. Dobrev, "Influence of bch and ldpc code parameters on the ber characteristic of satellite dvb channels," *Engineering, Technology amp; Applied Science Research*, vol. 4, no. 1, pp. 591–595, Feb. 2014. DOI: 10.48084/etasr.394. [Online]. Available: https://etasr.com/index.php/ETASR/article/view/394.

[11] O. Popescu, "Power budgets for cubesat radios to support ground communications and inter-satellite links," *IEEE Access*, vol. 5, pp. 12 618–12 625, 2017. DOI: 10.1109/ACCESS.2017.2721948.

[12] *Itu recommendation p.838-3: Specific attenuation model for rain for use in prediction methods*, International Telecommunication Union, 2005.

[13] *Itu recommendation p.837-7: Characteristics of precipitation for propagation modelling*, International Telecommunication Union, 2017.

[14] H. Schrank, "Antenna designer's notebook," *IEEE Antennas and Propagation Society Newsletter*, vol. 25, no. 4, pp. 28–29, 1983. DOI: 10.1109/MAP.1983.27697.

[15] R. Galuscak and P. Hazdra, "Circular polarization and polarization losses," Jan. 2006.

[16] *Itu recommendation p.372-13: Radio noise*, International Telecommunication Union, 2016.

[17] L. Joseffsson and P. Persson, in *Conformal Array Antenna Theory and Design*. John Wiley Sons, Ltd, 2006, ISBN: 9780471780120. DOI: https://doi.org/10.1002/047178012X.

[18] Y. Xia, B. Muneer, and Q. Zhu, "Design of a full solid angle scanning cylindrical-and-conical phased array antennas," *IEEE Transactions on Antennas and Propagation*, vol. 65, no. 9, pp. 4645–4655, 2017. DOI: 10.1109/TAP.2017.2730241.

[19] X. Ding, Y.-F. Cheng, X.-S. Yang, B.-Z. Wang, and D. E. Anagnostou, "A flush-mounted quasi-full-space beam-scanning cylindrical phased array," *IEEE Transactions on Antennas and Propagation*, vol. 67, no. 7, pp. 4883–4888, 2019. DOI: 10.1109/TAP.2019.2916457.

[20] J.-C. S. Chieh, E. Yeo, R. Farkouh, A. Castro, M. Kerber, R. B. Olsen, E. J. Merulla, and S. K. Sharma, "Development of flat panel active phased array antennas using 5g silicon rfics at ku- and ka-bands," *IEEE Access*, vol. 8, pp. 192 669–192 681, 2020. DOI: 10.1109/ACCESS.2020.3032841.

[21] X. Luo, J. Ouyang, Z.-H. Chen, Y. Yan, L. Han, Z. Wu, T. Yu, and K. Zheng, "A scalable ka-band 1024-element transmit dual-circularly-polarized planar phased array for satcom application," *IEEE Access*, vol. 8, pp. 156 084–156 095, 2020. DOI: 10.1109/ACCESS.2020.3019174.

[22] A. P. Lambert, "Thermal-mechanical analysis of system-level electronic packages for space applications," M.S. thesis, Montana State University - Bozeman, College of Engineering, 237 Norm Asbjornson Hall, Bozeman, MT 59717, United States of America, Nov. 2012. [Online]. Available: https://scholarworks.montana.edu/xmlui/handle/1/1696.

[23] Z. Xu, B. Ravelo, and O. Maurice, "Multiphysics tensorial network analysis applied to pcb interconnect fatigue under thermal cycle aggression," *IEEE Transactions on Electromagnetic Compatibility*, vol. 61, no. 4, pp. 1253–1260, 2019. DOI: 10.1109/TEMC.2019.2911873.

[24] K. K. Wei Low, S. Zihir, T. Kanar, and G. M. Rebeiz, "A scalable switchable dual-polarized 256-element ka-band satcom transmit phased-array with embedded rf driver and ±70° beam scanning," in *2020 IEEE/MTT-S International Microwave Symposium (IMS)*, 2020, pp. 821–824. DOI: 10.1109/IMS30576.2020.9223891.

[25] S. Parizi, "Bandwidth enhancement techniques," in. Nov. 2017, ISBN: 978-953-51-3601-9. DOI: 10.5772/intechopen.70173.

[26] J.-S. Row, "Design of aperture-coupled annular-ring microstrip antennas for circular polarization," *IEEE Transactions on Antennas and Propagation*, vol. 53, no. 5, pp. 1779–1784, 2005. DOI: 10.1109/TAP.2005.846809.

[27] J.-S. Row and J.-F. Wu, "Aperture-coupled microstrip antennas with switchable polarization," *IEEE Transactions on Antennas and Propagation*, vol. 54, no. 9, pp. 2686–2691, 2006. DOI: 10.1109/TAP.2006.880785.

[28] V. Balusa, V. S. K. P. Kumar, and B. T. P. Madhav, "Aperture coupled feed circularly polarized antenna," in *2015 International Conference on Signal Processing and Communication Engineering Systems*, 2015, pp. 240–244. DOI: 10.1109/SPACES.2015.7058257.

[29] G. Ganaraj, C. Kumar, V. S. Kumar, and Shankaraiah, "High gain circularly polarized resonance cavity antenna at x-band," in *2017 IEEE International Conference on Antenna Innovations Modern Technologies for Ground, Aircraft and Satellite Applications (iAIM)*, 2017, pp. 1–5. DOI: 10.1109/IAIM.2017.8402554.

[30] J. M. Llull Coll, "X-band antenna for cubesat satellite," Ph.D. dissertation, UPC, Escola Tècnica Superior d'Enginyeria de Telecomunicació de Barcelona, Departament de Teoria del Senyal i Comunicacions, 2017. [Online]. Available: http://hdl.handle.net/2117/100554.

[31] M. Zinieris, R. Sloan, and L. Davis, "A broadband microstrip- to-slot-line transition," *Microwave and Optical Technology Letters*, vol. 18, pp. 339–342, 1998.

[32] L. Yang, L. Zhu, W.-W. Choi, and K.-W. Tam, "Wideband vertical microstrip-to-microstrip transition designed with cross-coupled microstrip/slotline resonators," in *2015 Asia-Pacific Microwave Conference (APMC)*, vol. 2, 2015, pp. 1–3. DOI: 10.1109/APMC.2015.7413129.

[33] Z. Tao, J. Zhu, T. Zuo, L. Pan, and Y. Yu, "Broadband microstrip-to-microstrip vertical transition design," *IEEE Microwave and Wireless Components Letters*, vol. 26, no. 9, pp. 660–662, 2016. DOI: 10.1109/LMWC.2016.2597234.

[34] L. Yang, L. Zhu, W.-W. Choi, K.-W. Tam, R. Zhang, and J. Wang, "Wideband microstrip-to-microstrip vertical transition with high filtering selectivity using open-circuited slotline sir," *IEEE Microwave and Wireless Components Letters*, vol. 27, no. 4, pp. 329–331, 2017. DOI: 10.1109/LMWC.2017.2678423.

[35] L. Yang, L. Zhu, W.-W. Choi, and K.-W. Tam, "Novel microstrip-to-microstrip vertical transition designed with slotline stepped-impedance resonator," in *2018 International Conference on Microwave and Millimeter Wave Technology (ICMMT)*, 2018, pp. 1–3. DOI: 10.1109/ICMMT.2018.8563611.

[36] J. Huang, "A technique for an array to generate circular polarization with linearly polarized elements," *IEEE Transactions on Antennas and Propagation*, vol. 34, no. 9, pp. 1113–1124, 1986. DOI: 10.1109/TAP.1986.1143953.

UNIVERSITÉ CATHOLIQUE DE LOUVAIN
École polytechnique de Louvain
Rue Archimède, 1 bte L6.11.01, 1348 Louvain-la-Neuve, Belgique | **www.uclouvain.be/epl**